

November 8, 2022

Analytical Formulation and Field-Theoretic Simulation of Sequence-Specific Phase Separation of Proteinlike Heteropolymers with Short- and Long-Spatial-Range Interactions

Jonas WESSÉN, Suman DAS, Tanmoy PAL, and Hue Sun CHAN*

Department of Biochemistry, University of Toronto, Toronto, Ontario M5S 1A8, Canada

*Corresponding author

E-mail: huesun.chan@utoronto.ca; Tel: (416)978-2697; Fax: (416)978-8548

URL: <http://biochemistry.utoronto.ca/person/hue-sun-chan/>

Mailing address:

Department of Biochemistry, University of Toronto, Medical Sciences Building – 5th Fl.,
1 King's College Circle, Toronto, Ontario M5S 1A8, Canada.

Accepted for publication in *J Phys Chem B* as an article in the upcoming
"José Onuchic Festschrift" Special Issue

Abstract

A theory for sequence dependent liquid-liquid phase separation (LLPS) of intrinsically disordered proteins (IDPs) in the study of biomolecular condensates is formulated by extending the random phase approximation (RPA) and field-theoretic simulation (FTS) of heteropolymers with spatially long-range Coulomb interactions to include the fundamental effects of short-range, hydrophobic-like interactions between amino acid residues. To this end, short-range effects are modeled by Yukawa interactions between multiple non-electrostatic charges derived from an eigenvalue decomposition of pairwise residue-residue contact energies. Chain excluded volume is afforded by incompressibility constraints. A mean-field approximation leads to an effective Flory χ parameter, which, in conjunction with RPA, accounts for the contact-interaction effects of amino acid composition and the sequence-pattern effects of long-range electrostatics in IDP LLPS, whereas FTS based on the formulation provides full sequence dependence for both short- and long-range interactions. This general approach is illustrated here by applications to variants of a natural IDP in the context of several different amino-acid interaction schemes as well as a set of different model hydrophobic-polar sequences sharing the same composition. Effectiveness of the methodology is verified by coarse-grained explicit-chain molecular dynamics simulations.

INTRODUCTION

Tremendous recent advances have made it abundantly clear that biomolecular condensates serve many important biological functions.^{1–3} The architecture of functional intraorganismic biomolecular condensates can be highly complex. Some contain hundreds of different kinds of proteins—including folded protein domains, intrinsically disordered proteins (IDPs) and intrinsically disordered protein regions (IDRs)—and various nucleic acids participating in an intricate network of interactions, as exemplified by the ~ 300 protein species identified from proteomic analyses of yeast and mammalian stress granules using mass spectrometry.⁴ While the existence of intracellular liquid-like compartments has been suggested more than 120 years ago from observing that the protoplasm of starfish and sea urchin eggs resembles “a mixture of liquids” with suspended droplets of different chemical nature,⁵ the intense modern interest in biomolecular condensates was sparked by the recognition that the assembly of these condensates bears close resemblance to the physical process of liquid-liquid phase separation (LLPS)—as noted in a seminal study of germline P granules a little more than a decade ago.⁶ The LLPS perspective has since contributed greatly to the discovery and understanding of a large variety of biomolecular condensates. Progress is often achieved through experimental characterizations of the phase behaviors as well as the biochemical and materials properties of constructs, composing of only a few species of protein and nucleic acid, to serve as models of the biomolecular condensates of interest.^{7–17} One novel observation from these investigations is that multivalent, relatively weak interactions of IDPs and IDRs—typically weaker than binding of folded domains—often play a major role in the formation of biomolecular condensates.^{8–10,12} These interactions among largely disordered conformations of IDPs and IDRs are transient and presumably nonstoichiometric,^{18,19} though in some instances they entail sampling disordered chain configurations with labile but nonetheless specific fibril-like local structures^{8,20}. Despite the stochastic nature of these IDP/IDR interactions, they are capable of contributing to a “fuzzy”, sequence-dependent mechanism of molecular recognition.^{21,22}

Confronted by the overwhelming complexity of functional intraorganismic condensates, it goes without saying that few-component LLPS under thermodynamic equilibrium is a rudimentary—yet important—model for gaining insights into biomolecular condensates in living organisms. For instance, nonequilibrium behaviors of *in vivo* condensates are more appropriately viewed as those of active liquids;^{23,24} and formulations beyond simple LLPS theory are needed to describe the size, viscoelastic, and other materials properties of biomolecular condensates.^{25–27} In addition to physicochemical processes akin to LLPS, gelation and percolation^{28,29} as well as structure-specific stoichiometric interactions^{30,31} are expected to also contribute significantly to the formation of biomolecular condensates. It is likely that these processes are coupled³² as, at least in the example of a model condensate

for postsynaptic densities, stoichiometric interactions alone do not account for the experimentally observed phase properties.³³ Nonetheless, despite these complexities, since LLPS is integral to—though not exclusively responsible for—biomolecular condensate formation, experimental^{6–17} and theoretical/computational^{22,34–36,38–46} studies of equilibrium LLPS is a valuable tool for gaining physical, chemical, and biological insights. In this regard, they play an essential role similar to other simple model systems in many branches of science—including, as a befitting example for this Special Issue, a seminal lattice model study by Onuchic and coworkers⁴⁷ that inspired the funnel landscape picture of protein folding,^{48,49} with the obvious proviso that many aspects of the recent simple model LLPS systems’ quantitative relationship with the biological functions of intraorganismic biomolecular condensates remain to be delineated. Indeed, the LLPS perspective has already led to several notable conceptual advances, including a likely role of the general physical principle of phase separation in biomolecular homeostasis,^{22,29,50,51} novel clues to neurological effects of hydrostatic pressure,^{52,53} and a likely link between neurological disease-causing mutations and bioinformatics-inferred LLPS propensities,⁵⁴ to name a few.

Depending on the phenomena and scientific questions of interest, theoretical/computational modeling of biomolecular LLPS may endeavor to capture different levels of structural and energetic detail.²⁹ These modeling approaches include—but certainly not limited to—mean-field Flory-Huggins (FH)⁵⁵ and Overbeek-Voorn (OV)⁵⁶ theories of polymer solutions, random phase approximation (RPA) theories to address effects of sequence charge patterns on LLPS of polyampholytes as model IDPs/IDRs,^{36,38,57} field-theoretic simulation (FTS)⁵⁸ to provide an improved account of charge and matter density fluctuations beyond RPA for polyampholyte LLPS^{45,46,59,60}—though FTS is still limited by finite-size effects and in its treatment of excluded volume^{61–64}—as well as explicit-chain simulations of lattice,^{21,41,44,65} continuum coarse-grained,^{40,42,43,66–68} and atomistic^{69,70} models of IDP/IDR LLPS. Transfer matrix, restricted primitive model simulations, and other techniques have been applied to study complex coacervation of polyampholytes and polyelectrolytes;^{71–73} and LLPS of single or multiple biomolecular species, especially those involving folded proteins and folded domains, have also been modeled by patchy particles^{74–76} using simulations^{75,76} as well as analytical formalisms based on Wertheim’s thermodynamic perturbation theory.^{74,77} As expected, the required computation increases with structural and energetic details that a model seeks to capture. In this context, it is noteworthy that even basic FH theory, which requires minimal numerical effort⁷⁸ yet has recently been made even more tractable by a novel self-consistent solution,⁷⁹ can be very useful in advancing knowledge about biomolecular LLPS. This is exemplified by the applications of FH to delineate scenarios of tie-line patterns and their ramifications for homeostasis,^{22,29,51} to ascertain the extent of void-volume contributions to the hydrostatic pressure dependence of LLPS,⁵² and to rationalize experimental data on the impact of aromatic valence on IDP LLPS.⁸⁰

A fundamental limitation of mean-field FH and OV theories is that they consider the composition of heteropolymer sequences without accounting for the full effects of the sequential arrangements of monomers (e.g., amino acid residues for IDPs/IDRs) along heteropolymer chains. While explicit-chain simulations of LLPS readily embody sequence-pattern effects,^{40–44,66,69,70,81–85} theories that take into account sequence patterns but are computationally less intensive have proven useful as complementary approaches, especially for screening large number of sequences. To date, these sequence-specific theories, which include RPA, FTS, variational approaches,⁸⁶ and RPA augmented by Kuhn-length renormalization (rG-RPA)⁸⁷ for a more physical account of charge density and its fluctuations,⁸⁸ have focused only on spatially long-range Coulomb interactions entailed by the heteropolymeric sequence patterns of electric charges^{86,89,90} and their effects on LLPS,^{36,38,39,45,46,59,60,62,78,87,91,92} single-chain polyampholyte/IDP conformational properties,^{39,88,90,93–96} and the interaction of a pair of polyampholyte chains.⁸¹

These theoretical treatments of spatially long-range electrostatic interactions have led to many important physical insights; but these theories by themselves do not address the full sequence-dependent effects of spatially short-range, contact-like hydrophobic⁶⁹ and π -related^{97,98} interactions, which are integral parts of the physical driving forces for biomolecular LLPS^{40,66,69,98–101} as well as IDP conformational properties^{42,102,103} and interactions.⁹⁷ In lieu of an account of sequence-pattern dependence, short-range interactions are sometimes treated by augmenting a sequence-dependent theory for electrostatic interactions such as RPA by a composition-dependent mean-field FH account of spatially short-range interactions.^{36,38} One source of difficulty in extending RPA to include spatially short-range attractive (favorable) interactions is that they are prone to produce mathematical singularities in the RPA free energy, signalling the instability of the homogeneous phase about which the RPA expansion is performed. This observation led us to consider the possibility of incorporating these interactions in FTS because FTS does not require the approximations in RPA theory and should, therefore, properly handle the singularities. We put forth such a theory here. To account for nonelectrostatic, spatially short-range interactions in our FTS formulation, additional fields are introduced, wherein different amino acid residues are assigned different nonelectrostatic charges associated with the newly introduced fields. The nonelectrostatic charges are determined as components of eigenvectors using eigenvalue decomposition of the pairwise interaction energies^{104–107} from either the values for the 20 amino acids on a hydrophobicity (hydropathy) scale^{40,108–113} or the $20 \times 21/2 = 210$ pairwise contact energies between the amino acids (the interaction matrix) derived from statistical analyses of the Protein Data Bank (PDB) and/or from physical considerations.^{40,114–118} This approach is computationally tractable because matrices for physical pairwise interactions among amino acid residues tend to possess a dominant eigenvector.^{104–106,119,120} Thus, only a small number of types of nonelectric charge

($\ll 20$) are necessary to provide a mathematically good approximation to the 210 pairwise interactions. In view of the long-standing recognition that there are significant discrepancies among hydrophobicity scales because of differences in the experimental or computational techniques used for their construction,^{121–123} the size- and length-scale dependence of hydrophobic interactions^{124–126} and their deviations from pairwise additivity^{127–129} (as manifested, e.g., by the fact that pairwise interactions alone are insufficient to account for protein folding cooperativity^{127,130,131}), we apply our new formulation to several different hydrophobicity scales^{40,111,112} and pairwise interaction schemes^{40,117} to compare their predicted LLPS behaviors for the wildtype and variant IDRs of the DEAD-box RNA helicase Ddx4^{9,19} and two-letter (hydrophobic-polar) model sequences.^{132,133} The theoretical predictions are compared against experimental trend and corresponding predictions from coarse-grained explicit-chain molecular dynamics simulations. These results, together with their underpinning theoretical development and their ramifications for future efforts, are provided in detail below.

MODELS AND METHODS

We begin by presenting a general analytical formulation, amenable to RPA and FTS, for a model system containing multiple chains of heteropolymers with specific sequences of residues (monomers) together with small ions and solvent molecules, wherein the constituents may interact via spatially short-range, contact-like interactions as well as spatially long-range Coulomb interactions.

Spectral (Eigenvalue) Decomposition of Residue-Residue Energy Matrices and Definition of Nonelectric Charges. Assuming that the spatially short-range interactions among the twenty types of amino acid residues may be described approximately by a 20×20 matrix $\varepsilon_{r,r'}$ of contact energies for the pairwise interactions between residue types r and r' , this matrix can be written in the diagonalized form

$$\varepsilon_{r,r'} = \sum_{a=1}^{20} \lambda_a q^{(a)}_r q^{(a)}_{r'} \quad (1)$$

because $\varepsilon_{r,r'}$ is symmetric ($\varepsilon_{r,r'} = \varepsilon_{r',r}$), with $\{\lambda_a\}_{a=1}^{20}$ being the eigenvalues of $\varepsilon_{r,r'}$, and $q^{(a)}_r$ constituting a set of twenty orthogonal, unit-normalized eigenvectors labeled by a . We may then view the eigenvector component $q^{(a)}_r$ as the value of a mathematically defined type- a nonelectric charge for residue type r . Without loss of generality, we label the eigenvalues (and thus the nonelectric charge type) such that the eigenvalues are ordered according to descending magnitude, i.e., $|\lambda_a| \geq |\lambda_{a+1}|$.

The spectral form in Eq. (1) implies that we can decompose the full $\varepsilon_{r,r'}$ into a set of interactions, with overall strengths λ_a and relative residue-dependent strengths given by product of nonelectric charges $q^{(a)}_r q^{(a)}_{r'}$. Indeed, this approach has long been used to construct hydrophobicity scales using the eigenvalue decomposition of statistical contact potentials such as the classic Miyazawa-Jernigan (MJ) matrix.^{104,105,114,115}

Although all twenty eigenvalues are needed in Eq. (1) to recover the full $\varepsilon_{r,r'}$ exactly, one can often achieve a very good numerical agreement by including only the first few most dominant λ_a , i.e. by truncating the sum at some $\tilde{a} < 20$,

$$\sum_{a=1}^{20} \rightarrow \sum_{a=1}^{\tilde{a}}, \quad (2)$$

because of the pattern of hydrophobic-like interactions among amino acid residues.^{104–106,119,120} For our present purpose, we consider two interaction matrices proposed recently for the study of IDP LLPS, namely, $\varepsilon_{r,r'}^{\text{KH}}$ obtained through a shifted MJ matrix,^{40,115} and $\varepsilon_{r,r'}^{\text{Mpipi}}$, which is partly based on explicit-water simulations of pairwise amino acid residue interactions and has recently been used to successfully predict LLPS propensities of several biologically important IDPs¹¹⁷ (Fig. 1). The accuracies of truncated eigenvalue decompositions of $\varepsilon_{r,r'}^{\text{KH}}$ and $\varepsilon_{r,r'}^{\text{Mpipi}}$ [Eq. (2), with $\tilde{a} = 1, 2, 3, 4$, and 5] are illustrated in Fig. 1a,b and the associated nonelectric charges associated with the $a = 1, 2, 3, 4$, and 5 eigenvalues are provided in Fig. 1c.

Fig. 1 shows significant deviations from $\varepsilon_{r,r'}^{\text{KH}}$ or $\varepsilon_{r,r'}^{\text{Mpipi}}$ when only one eigenvalue is used ($\tilde{a} = 1$). At the same time, it indicates that eigenvalue decomposition is reasonably accurate for $\tilde{a} \geq 2$. Interestingly, for $\tilde{a} = 1$, i.e., when only a single nonelectric charge type is used to describe the interactions, large deviations are observed only for repulsive (> 0) interactions in KH but observed for strongly attractive (more negative) interactions as well as a subset of the less attractive interactions in Mpipi. When these two pairwise interaction schemes are compared, the nonelectric charges ($q^{(1)}_{rs}$) of the large nonpolar residues—valine, isoleucine, leucine, and methionine—associated with the energy matrix’s most dominant ($a = 1$) eigenvalue is much higher in KH than in Mpipi, reflecting the weaker interactions among these nonpolar residues ascribed by Mpipi than by KH. But the corresponding nonelectric charges for the aromatic residues phenylalanine, tyrosine, and tryptophan are higher in Mpipi than in KH, reflecting the relatively more favorable interactions enjoyed by these residues in Mpipi than in KH (see below). As previously recognized,^{104,105,120} at least for KH, the nonelectric charge associated with the most dominant eigenvalue corresponds to a measure of hydrophobicity, with polar residues having smaller $q^{(1)}_{rs}$ and large nonpolar residues having larger $q^{(1)}_{rs}$ (red bars in the top panel of Fig.1c). While all $a = 1$ nonelectric charges are positive, $q^{(a)}_{rs}$ can take positive and negative values for $a \geq 2$. Intuitively, for KH, the nonelectric charge for $a = 2$ corresponds to a measure of polarity, with most polar residues

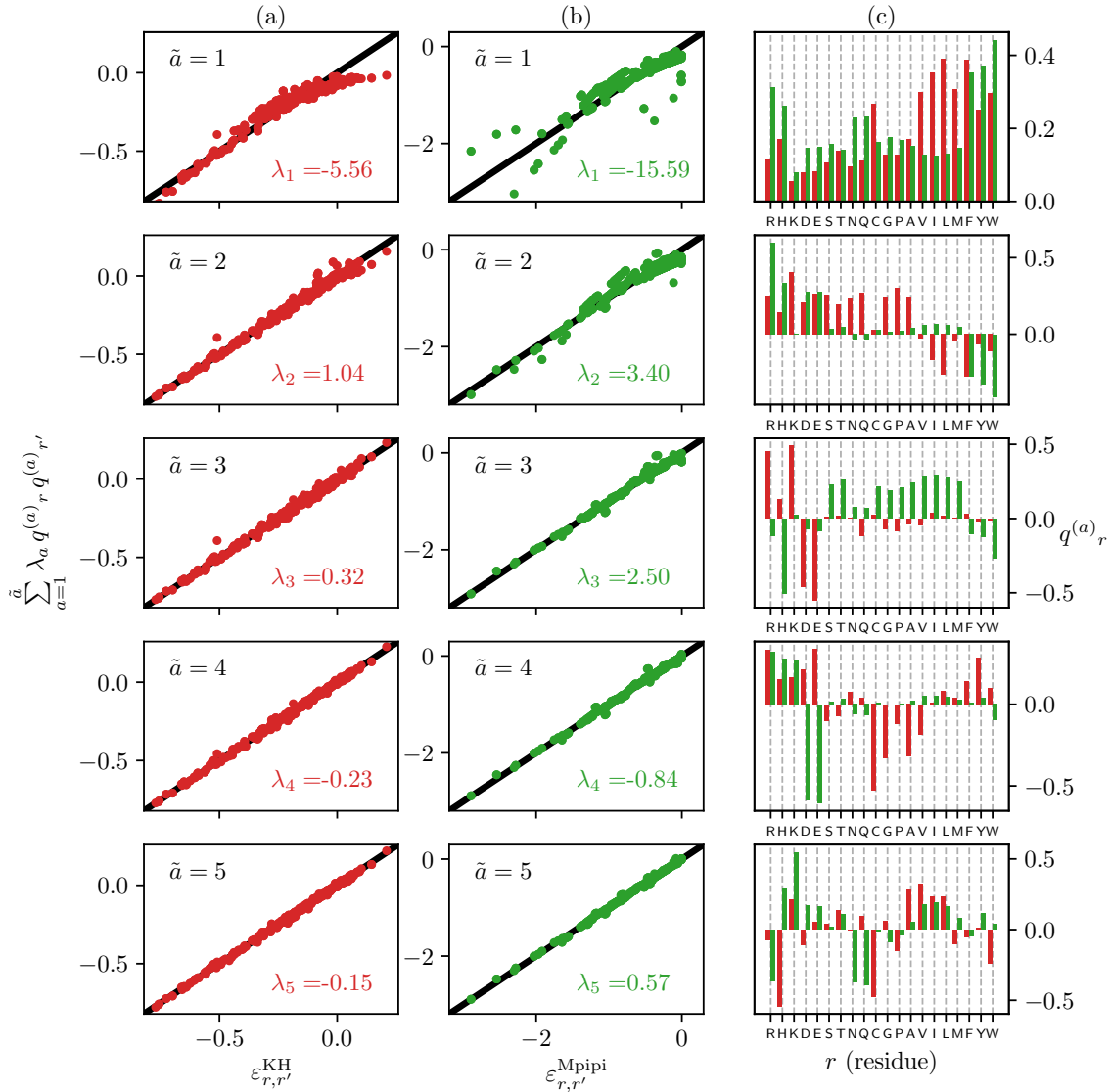


Fig. 1: Eigenvalue decomposition of (a) $\epsilon_{r,r'}^{\text{KH}}$ and (b) $\epsilon_{r,r'}^{\text{Mpipi}}$ using Eqs. (1) and (2) where the summations over eigenvalues are truncated at \tilde{a} . Accuracy of a set of truncated summations (vertical variable) is indicated by the proximity of the scatter plot [red (a) and green (b) data points] to the slope = 1 black line through the origin. (c) Nonelectric charges $q^{(a)}_r$, $a = 1, 2, 3, 4$, and 5 (top to bottom) of the amino acid residue types (shown by their standard one-letter codes) are displayed for KH (red) and Mpipi (green). For KH, $\epsilon_{r,r'}^{\text{KH}}$ values [horizontal variable in (a)] are taken from Table S3 of ref. 40 (corresponding to the “KH-D” model in this reference). For Mpipi, $\epsilon_{r,r'}^{\text{Mpipi}}$ values [horizontal variable in (b)] are the contact energies given in Supplementary Table 11 of ref. 117.

having $q^{(2)}_r > 0$ and most nonpolar residues having $q^{(2)}_r < 0$; and the nonelectric charge for $a = 3$ appears to correlate strongly with electric charge, with arginine and lysine having the largest (most positive) $q^{(3)}_{r,s}$ whereas aspartic and glutamic acids having the most negative $q^{(3)}_{r,s}$ (second and third panels from the top of Fig.1c). These observations are tentativ-

ing, but it should be emphasized that the nonelectric charges are basically mathematical constructs. As such, they do not always lend themselves to simple interpretations in terms of physical interaction types. A case in point is that the corresponding trend of $q^{(2)}_r$ and $q^{(3)}_r$ values in Mpipi is less straightforward to interpret in terms of a particular physical characteristics of the amino acid residues.

Besides KH and Mpipi, we consider three representative interaction matrices constructed from hydrophobicity scales that have recently been used for simulations of single-IDP conformations and biomolecular LLPS. We refer to these interaction matrices as (i) $\varepsilon_{r,r'}^{\text{HPS}}$, which is derived in ref. 40 from an OPLS (optimized potentials for liquid simulations) forcefield-based hydrophobicity scale,¹⁰⁸ (ii) $\varepsilon_{r,r'}^{\text{Urry}}$, which is derived in ref. 111 from a prior analysis by Urry et al. of experimental data on heat-induced conformational compaction of host-guest polypeptides,¹⁰⁹ and (iii) $\varepsilon_{r,r'}^{\text{FB}}$, which is derived in ref. 112 by optimizing agreement between coarse-grained molecular dynamics simulations based on putative hydrophobicity scales with experimental data on the radii of gyration of single-chain IDP conformational ensembles (a similar approach was also utilized in ref. 113). These interaction matrices take the general form

$$\varepsilon_{r,r'}^X = \frac{\tilde{\lambda}_r + \tilde{\lambda}_{r'}}{2} + \Delta, \quad X = \text{HPS, Urry, FB}, \quad (3)$$

where $\tilde{\lambda}_r$ are twenty residue-specific hydrophobicity/hydrophathy values [not to be confused with the eigenvalues λ_a in Eq. (1)] and Δ is an overall shift. Matrices in the form of Eq. (3) have at most two nonzero eigenvalues, given by $\lambda_{1,2} = \frac{1}{2} \left[\sum_r \tilde{\lambda}_r + \Delta \pm \sqrt{20 \sum_r (\tilde{\lambda}_r + \Delta)^2} \right]$. A visual impression of the similarities and differences among the five interaction matrices considered in this work are provided by their depiction in Fig. 2 as heat maps.

It follows from the above discussion that formulation of the interactions entailed by HPS, Urry, and FB by eigenvalue decomposition in terms of nonelectric charges are straightforward because it requires at most two types of nonelectric charges. By comparison, the accuracy of corresponding formulations using a small number of types of nonelectric charges for interaction schemes encoded by 20×20 energy matrices that are not derived from a 20-value hydrophobicity scale (such as KH and Mpipi) has to be ascertained. In Fig. 3, the accuracy of the truncated eigenvalue decompositions of $\varepsilon_{r,r'}^{\text{KH}}$ and $\varepsilon_{r,r'}^{\text{Mpipi}}$ is assessed by considering the quantity

$$\Delta\varepsilon_{r,r'} = \sum_{a=1}^{\tilde{a}} \lambda_a q^{(a)}_r q^{(a)}_{r'} - \varepsilon_{r,r'}, \quad (4)$$

which is the difference between the truncated summation and the original $\varepsilon_{r,r'}$. Results for KH and Mpipi at $\tilde{a} = 1, 2$, and 3 are shown, respectively, in Fig. 3a, b, and c. The heat maps in Fig. 3 indicate that the KH interaction matrix is very well approximated at $\tilde{a} = 3$ with the only exception of the cysteine–cysteine (C–C) entry, which is noticeably overestimated at all $\tilde{a} \leq 3$. This exception is in line with the fact that the covalent C–C disulfide bond

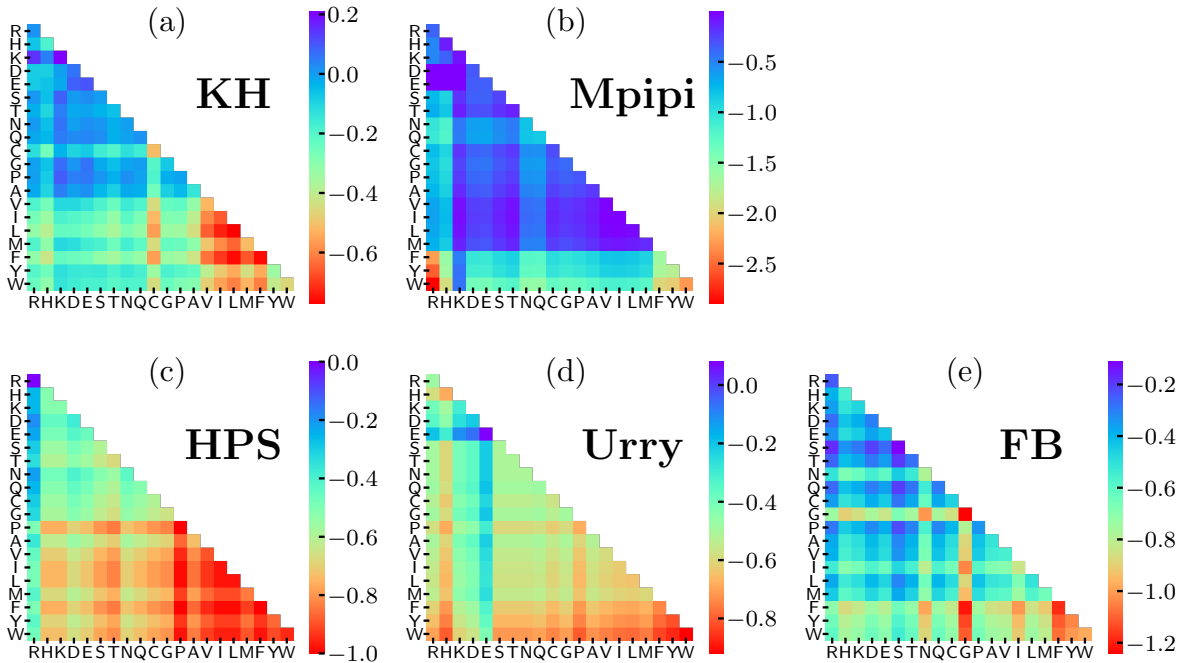


Fig. 2: Heat-map representations of the interaction matrices considered in the present work: (a) $\varepsilon_{r,r'}^{\text{KH}}$, (b) $\varepsilon_{r,r'}^{\text{Mpipi}}$, (c) $\varepsilon_{r,r'}^{\text{HPS}}$, (d) $\varepsilon_{r,r'}^{\text{Urry}}$, and (e) $\varepsilon_{r,r'}^{\text{FB}}$. The color scale ranges from red (most attractive) to blue (least attractive or most repulsive). The HPS, Urry and FB matrices follow from Eq. (3) where the values of $\tilde{\lambda}_r$ are taken from Table S1 in ref. 40 for HPS, Table S2 in ref. 111 for Urry, and Table S7 in ref. 112 for FB. Overall shift $\Delta = 0$ for both HPS and FB, whereas $\Delta = 0.08$ for Urry. Corresponding information for $\varepsilon_{r,r'}^{\text{KH}}$ and $\varepsilon_{r,r'}^{\text{Mpipi}}$ is provided in the caption of Fig. 1.

is physically different from all the other pairwise residue contacts that are noncovalent in nature. Disulfide bonds are significantly more important in folded proteins than in IDPs. This may be a reason why the C–C exception in the accuracy of eigenvalue decomposition is observed in PDB-derived KH but not in the IDP physics/bioinformatics-derived Mpipi. For Mpipi, the truncated eigenvalue decomposition at $\tilde{a} = 3$ is reasonably accurate though it overestimates interactions involving the electrically negative aspartic and glutamic acid residues.

Under the next subheading, we will use the eigenvalue decomposition in Eq. (1) to derive a statistical field theory for protein solutions with spatially short-range residue-dependent interactions governed by a matrix of contact energies $\varepsilon_{r,r'}$. Relative to the field theory we consider previously for polyampholytes,^{62,78,91,92} the present extended field theory contains \tilde{a} additional fields, i.e., one additional field $\varphi_a(\mathbf{r})$ for every eigenvalue λ_a included, wherein the field $\varphi_a(\mathbf{r})$ is conjugate to the density of nonelectric charges $q^{(a)}_r$. Under subsequent subheadings, the new theory is first studied using an approximate analytical approach we find useful for computationally efficient comparisons of interaction schemes encoded by different $\varepsilon_{r,r'}$ s. The theory is then explored using FTS to take into complete account of field

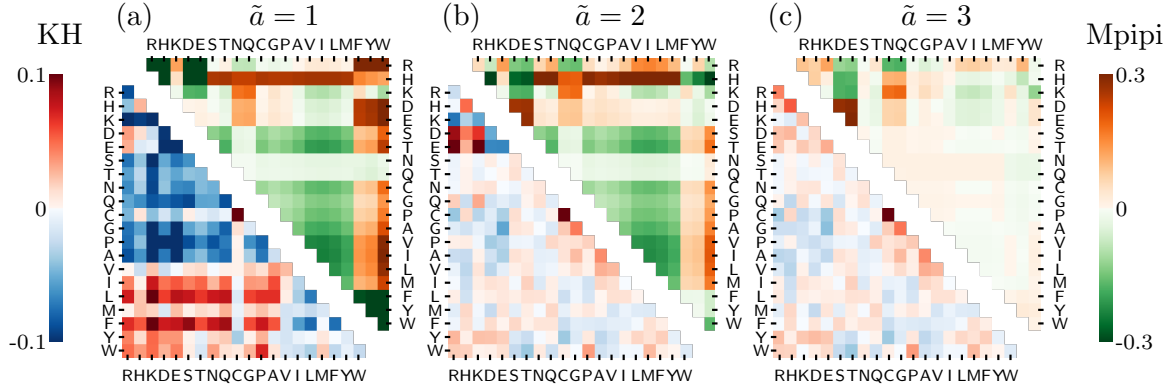


Fig. 3: Accuracy of the truncated eigenvalue decomposition of 20×20 interaction matrices that are not derived from 20-value hydrophobicity scales. The level of accuracy for $\tilde{a} = 1, 2$, and 3 (a–c) is quantified by $\Delta\varepsilon_{r,r'}$ in Eq. (4). Bottom-left triangles using the blue–red color scale on the left display $\Delta\varepsilon_{r,r'}$ for KH, whereas top-right triangles using the green–orange color scale on the right display the same quantity for Mpipi.

fluctuations so as to provide, in the context of the present model, full sequence dependence of biomolecular LLPS and detailed structural information about residue partitioning inside protein-dense condensates.

Statistical Field Theory. Here we consider a system of volume V with n_p protein chains, each consisting of N consecutive amino acid residues of types r_α (with $\alpha = 1, \dots, N$), and denote the position of residue α on chain i ($= 1, \dots, n_p$) as $\mathbf{R}_{i,\alpha}$. The system contains also n_+ unit-positive and n_- unit-negative ions with positions $\mathbf{r}_{\pm,i}$, and n_w neutral solvent particles with positions $\mathbf{r}_{w,i}$. We let $\rho_{p,\pm,w} \equiv n_{p,\pm,w}/V$ denote the bulk number densities of the polymers, ions and solvent in the system, and $\rho_b = Nn_p/V = N\rho_p$ the bulk number density of polymer beads. The canonical partition function of this system is given by

$$Z = \frac{1}{n_p!n_+!n_-!n_w!} \int \{d\mathbf{R}\} \{d\mathbf{r}_+\} \{d\mathbf{r}_-\} \{d\mathbf{r}_w\} e^{-\hat{H}}, \quad (5)$$

where

$$\{d\mathbf{R}\} \equiv \prod_{i=1}^{n_p} \prod_{\alpha=1}^N d\mathbf{R}_{i,\alpha}, \quad \{d\mathbf{r}_\pm\} \equiv \prod_{i=1}^{n_\pm} d\mathbf{r}_{\pm,i}, \quad \{d\mathbf{r}_w\} \equiv \prod_{i=1}^{n_w} d\mathbf{r}_{w,i} \quad (6)$$

are position integration measures for polymer beads, ions and solvents, respectively. The microscopic Hamiltonian in units of $k_B T$, where k_B is Boltzmann’s constant and T is absolute temperature, written as

$$\hat{H} = \hat{H}_0 + \hat{H}_c + \hat{H}_e + \hat{H}_h, \quad (7)$$

contains terms accounting for chain connectivity (\hat{H}_0), soft compressibility (\hat{H}_c), electrostatic interactions (\hat{H}_e) and spatially short-range hydrophobic-like interactions—which may

include van der Waals, π -related, and other forms of short-spatial-range interactions (\hat{H}_h). The chain connectivity term

$$\hat{H}_0 = \frac{3}{2b^2} \sum_{i=1}^{n_p} \sum_{\alpha=1}^{N-1} (\mathbf{R}_{i,\alpha+1} - \mathbf{R}_{i,\alpha})^2 \quad (8)$$

is controlled by the segment length b which we set to the trans C_α - C_α virtual bond length, i.e., $b = 3.8 \text{ \AA}$, throughout this work. The soft-compressibility term

$$\hat{H}_c = \frac{1}{2\gamma} \int d\mathbf{r} [\hat{\rho}(\mathbf{r}) - \rho_0]^2 \quad (9)$$

penalizes deviations of the total density

$$\hat{\rho}(\mathbf{r}) = v_b \hat{\rho}_b(\mathbf{r}) + v_+ \hat{\rho}_+(\mathbf{r}) + v_- \hat{\rho}_-(\mathbf{r}) + v_w \hat{\rho}_w(\mathbf{r}) \quad (10)$$

from a reference density ρ_0 , and thus serves to capture an essential aspect of excluded volume effects. In the above equation, $\hat{\rho}_i(\mathbf{r})$ with $i = b, +, -, w$ (referring to polymer bead, cation, anion, and solvent particle, respectively) is the number density of species i at position \mathbf{r} and the v_i s are factors that we use to model the relative volume of the different particles. The number densities are

$$\hat{\rho}_b(\mathbf{r}) = \sum_{i=1}^{n_p} \sum_{\alpha=1}^N \Gamma(\mathbf{r} - \mathbf{R}_{i,\alpha}) \quad \text{and} \quad \hat{\rho}_i(\mathbf{r}) = \sum_{j=1}^{n_i} \Gamma(\mathbf{r} - \mathbf{r}_{i,j}), \quad i = +, -, w, \quad (11)$$

where individual particles are modeled as Gaussian distributions $\Gamma(\mathbf{r}) = e^{-\mathbf{r}^2/2a_s^2}/(2\pi a_s^2)^{3/2}$, which serve to regularize infinities arising from particle contact interactions and self interactions.^{135,136} Here the smearing parameter a_s is equal to $1/\sqrt{3}$ of the standard deviation of \mathbf{r} in the $\Gamma(\mathbf{r})$ distribution (i.e., $a_s = \sqrt{\langle |\mathbf{r}|^2 \rangle / 3}$). We refer to γ in Eq. (9)—which has units of density—as the compressibility, and note that in the limit of $\gamma \rightarrow 0$, we obtain the standard incompressibility condition $e^{-\hat{H}_c} \propto \delta[\hat{\rho}(\mathbf{r}) - \rho_0]$ where the functional δ -function enforces $\hat{\rho}(\mathbf{r}) = \rho_0$ at all spatial positions \mathbf{r} .

Electrostatic interactions are included in \hat{H}_e through the standard pairwise Coulomb potential,

$$\hat{H}_e = \frac{l_B}{2} \int d\mathbf{r} \int d\mathbf{r}' \frac{\hat{c}(\mathbf{r})\hat{c}(\mathbf{r}')}{|\mathbf{r} - \mathbf{r}'|}, \quad (12)$$

where

$$\hat{c}(\mathbf{r}) = \sum_{i=1}^{n_p} \sum_{\alpha=1}^N \sigma_{i,\alpha} \Gamma(\mathbf{r} - \mathbf{R}_{i,\alpha}) + \hat{\rho}_+(\mathbf{r}) - \hat{\rho}_-(\mathbf{r}) \quad (13)$$

is the density of electric charge at \mathbf{r} and $\sigma_{i,\alpha}$ is the electric charge of the α th residue on the

i th chain in units of the proton charge e . Because the present study is limited to systems of chains with identical sequence, i.e., $\sigma_{i,\alpha} = \sigma_\alpha$ is independent of i , the subscript i will be dropped from the symbol σ for electric charge hereafter. The strength of electrostatic interactions is controlled by the Bjerrum length $l_B = e^2/4\pi\epsilon_0\epsilon_r k_B T$ that involves vacuum permittivity ϵ_0 and a constant background relative permittivity ϵ_r . In this work, we neglect any concentration dependence of ϵ_r as this has been shown to amount to only small to moderate effects on LLPS propensity.⁹¹ Nonetheless, if desired, it would be straightforward to implement a concentration dependent permittivity in our model through the approach described in ref. 91.

The final term in the Hamiltonian in Eq. (7), \hat{H}_h , contains the pairwise residue-specific spatially short-range interactions, which we express as

$$\hat{H}_h = \frac{1}{2} \sum_{i,j=1}^{n_p} \sum_{\alpha,\beta=1}^N \varepsilon_{r_\alpha,r_\beta} \Gamma^2 \star V_h(|\mathbf{R}_{i,\alpha} - \mathbf{R}_{j,\beta}|) \quad (14)$$

where

$$\Gamma^2 \star V_h(|\mathbf{R}_{i,\alpha} - \mathbf{R}_{j,\beta}|) \equiv \int d\mathbf{r} \int d\mathbf{r}' \Gamma(\mathbf{r} - \mathbf{R}_{i,\alpha}) \Gamma(\mathbf{r}' - \mathbf{R}_{j,\beta}) V_h(|\mathbf{r} - \mathbf{r}'|) \quad (15)$$

accounts for the residue-residue interaction in the presence of Gaussian smearing (note that $\Gamma^2 \star V_h \rightarrow V_h$ as $a_s \rightarrow 0$). Leaving the functional form of the interaction potential $V_h(|\mathbf{r}|)$ (in units of $k_B T$) unspecified for the moment, we have in the above expression assumed that all residue dependence is accounted for by the overall multiplicative factors $\varepsilon_{r_\alpha,r_\beta}$ from a given interaction matrix. The spectral form of $\varepsilon_{r,r'}$ in Eq. (1) can be used to write \hat{H}_h in Eq. (14) as

$$\hat{H}_h = \sum_{a=1}^{20} \frac{1}{2} \int d\mathbf{r} \int d\mathbf{r}' V_h(|\mathbf{r} - \mathbf{r}'|) \lambda_a \hat{h}_a(\mathbf{r}) \hat{h}_a(\mathbf{r}'), \quad (16)$$

where

$$\hat{h}_a(\mathbf{r}) = \sum_{i=1}^{n_p} \sum_{\alpha=1}^N q^{(a)}_{r_\alpha} \Gamma(\mathbf{r} - \mathbf{R}_{i,\alpha}) \quad (17)$$

is the density of nonelectric charge for the a th eigenvalue λ_a at position \mathbf{r} .

The Hamiltonian terms $\hat{H}_{c,e,h}$ for non-bonded interactions are quadratic in densities and can thus be decoupled using standard Hubbard-Stratonovich transformations,⁵⁸ turning the partition function in Eq. (5) into that of a statistical field theory. Special care needs to be given to \hat{H}_h wherein terms with $\lambda_a > 0$ and $\lambda_a < 0$ need to be linearized with fields integrated on the imaginary and real axis, respectively. To keep track of the sign of eigenvalue λ_a , we

introduce the variable ξ_a , defined as

$$\xi_a = \begin{cases} -i & , \lambda_a < 0 \\ 1 & , \lambda_a > 0 \end{cases}, \quad (18)$$

where $i^2 = -1$. The partition function Z in Eq. (5) can then be shown to be equivalent to a statistical field theory with partition function

$$Z = \frac{V^{n_p+n_++n_-+n_w}}{n_p!n_+!n_-!n_w!} \int \mathcal{D}\eta \int \mathcal{D}\psi \left(\prod_{a=1}^{20} \int \mathcal{D}\varphi_a \right) e^{-H[\eta, \psi, \{\varphi_a\}]}, \quad (19)$$

where the field Hamiltonian (in units of $k_B T$)

$$H = - \sum_{i=p,+, -, w} n_i \ln Q_i[\check{\eta}, \check{\psi}, \{\check{\varphi}_a\}] + \int d\mathbf{r} \left[-i\rho_0\eta + \frac{\gamma\eta^2}{2} + \frac{(\nabla\psi)^2}{8\pi l_B} + \sum_{a=1}^{20} \frac{\varphi_a V_h^{-1} \varphi_a}{2|\lambda_a|} \right]. \quad (20)$$

In the field theory representation of the system, $\eta(\mathbf{r})$ and $\psi(\mathbf{r})$ are conjugate fields to the density $\hat{\rho}(\mathbf{r})$ and the electric charge density $\hat{c}(\mathbf{r})$, respectively, while $\varphi_a(\mathbf{r})$ is conjugate to the nonelectric charge density $\hat{h}_a(\mathbf{r})$ associated with eigenvalue λ_a in the spectral decomposition of the interaction matrix. The single-molecule partition functions $Q_{p,\pm,w}[\check{\eta}, \check{\psi}, \{\check{\varphi}_a\}]$ depend on smeared fields $\check{\phi}(\mathbf{r}) = \Gamma \star \phi(\mathbf{r}) \equiv \int d\mathbf{r}' \Gamma(\mathbf{r} - \mathbf{r}') \phi(\mathbf{r}')$ (for $\phi = \eta, \psi, \varphi_a$) via the relations

$$Q_{\pm} = \frac{1}{V} \int d\mathbf{r} \exp \left[-i(v_{\pm} \check{\eta}(\mathbf{r}) \pm \check{\psi}(\mathbf{r})) \right], \quad (21)$$

$$Q_w = \frac{1}{V} \int d\mathbf{r} \exp [-iv_w \check{\eta}(\mathbf{r})] \quad (22)$$

for ions and solvents, respectively, and

$$Q_p = \frac{1}{\mathcal{N}} \left(\prod_{\alpha=1}^N \int d\mathbf{R}_{\alpha} \right) \exp \left[-\frac{3}{2b^2} \sum_{\alpha=1}^{N-1} (\mathbf{R}_{\alpha+1} - \mathbf{R}_{\alpha})^2 - \sum_{\alpha=1}^N W_{\alpha}(\mathbf{R}_{\alpha}) \right] \quad (23)$$

for polymer chains, where $\mathcal{N} \equiv V(2\pi b^2/3)^{3(N-1)/2}$ normalizes Q_p to unity at zero field values, and

$$W_{\alpha}(\mathbf{r}) = iv_b \check{\eta}(\mathbf{r}) + i\sigma_{\alpha} \check{\psi}(\mathbf{r}) + \sum_{a=1}^{20} i \xi_a q^{(a)} r_{\alpha} \check{\varphi}_a(\mathbf{r}). \quad (24)$$

In Eq. (20), V_h^{-1} represents a differential operator satisfying

$$V_h^{-1} V_h(|\mathbf{r}|) = \delta(\mathbf{r}) \quad (25)$$

and thus V_h^{-1} depends on the functional form of $V_h(|\mathbf{r}|)$. Since our primary goal here is formulation development, for simplicity we consider only temperature-independent forms of the spatially short-range interaction potential $V_h(|\mathbf{r}|)$. Physically, however, solvent-mediated interactions of amino acid residues can be temperature dependent when viewed in an implicit-solvent perspective,²⁹ especially for the hydrophobic effects among nonpolar residues,⁴⁹ leading, e.g., to cold denaturation¹³⁷ and LLPS driven by increasing temperature rather than decreasing temperature.¹⁶ When necessary, these effects can be readily incorporated into our formulation by introducing temperature-dependent potentials,^{49,137,138} i.e., $V_h(|\mathbf{r}|) \rightarrow V_h(|\mathbf{r}|, T)$ as in ref. 139.

Analytical Calculation of the Leading Order Free Energy. We next proceed to an approximate evaluation of the statistical field theory partition function Z in Eq. (19). In the analytical approach taken here, we only account for the leading-order effects from each field around the homogeneous saddle solution. For our model, this amounts to the mean field theory (MFT) solution for the fields η and φ_a , while electrostatic effects first show up at the one-loop level in ψ which are accounted for by RPA.

The spatially homogeneous MFT solution is obtained by first letting the fields η , ψ and φ_a in the expression for the field Hamiltonian H in Eq. (20) be position-independent (hence smeared fields $\check{\phi} = \phi$ for $\phi = \eta, \psi, \varphi_a$ are also position-independent) and then requiring that the first derivatives of the resulting H with respect to the fields are zero. With position-independent fields, the single-molecule partition functions Q_i , defined in Eqs. (21)–(23), become

$$\begin{aligned} Q_w &= e^{-iv_w\eta}, \\ Q_{\pm} &= e^{-iv_{\pm}\eta \mp i\psi}, \\ Q_p &= \exp \left[-iNv_b\eta - i\sigma_p\psi - i \sum_{a=1}^{20} \xi_a q^{(a)} \varphi_a \right], \end{aligned} \tag{26}$$

where $\sigma_p = \sum_{\alpha=1}^N \sigma_{\alpha}$ is the net charge of a polymer and $q^{(a)} = \sum_{\alpha=1}^N q^{(a)}_{r_{\alpha}}$ is the total nonelectric charge associated with the a th eigenvalue of one polymer chain. The above relations for Q_i lead to the following expression for H with homogeneous fields:

$$\begin{aligned} H &= i(n_p N n_b + n_+ v_+ + n_- v_- + n_w v_w) \eta + i(n_p \sigma_p + n_+ - n_-) \psi + i n_p \sum_{a=1}^{20} \xi_a q^{(a)} \varphi_a \\ &+ V \left[-i\rho_0 \eta + \frac{\gamma \eta^2}{2} + \sum_{a=1}^{20} \frac{\varphi_a^2}{2|\lambda_a| \hat{V}_h(\mathbf{0})} \right]. \end{aligned} \tag{27}$$

In Eq. (27), $\hat{V}_h(\mathbf{0})$ is the $\mathbf{k} = \mathbf{0}$ component of the Fourier transform $\hat{V}_h(\mathbf{k}) = \int d\mathbf{r} e^{-i\mathbf{r}\cdot\mathbf{k}} V_h(|\mathbf{r}|)$ of the spatially short-range potential $V_h(|\mathbf{r}|)$. This factor can be derived by considering the

Fourier representation of $\delta(\mathbf{r}) = (2\pi)^{-3} \int d\mathbf{k} \exp(i\mathbf{k} \cdot \mathbf{r})$ in the defining Eq. (25) for V_h^{-1} , which leads to $V_h^{-1} \exp(i\mathbf{k} \cdot \mathbf{r}) = \exp(i\mathbf{k} \cdot \mathbf{r})/\hat{V}_h(\mathbf{k})$. Then, by noting that the Fourier transform of the position-independent φ_a is proportional to $\delta(\mathbf{k})$, it is straightforward to show that the $\int d\mathbf{r}$ integration with position-independent φ_a produces the $\hat{V}_h(\mathbf{0})$ term.

The coefficient of $i\psi$ in Eq. (27) is the total electric charge in the system which must be set to zero, $n_p\sigma_p + n_+ - n_- = 0$. The charge-conjugate field ψ thus vanishes in Eq. (27) with no contribution to the MFT solution. For the other fields, solving $\partial H/\partial\eta = \partial H/\partial\varphi_a = 0$ for $\bar{\eta}$ and $\bar{\varphi}_a$ leads to

$$\bar{\eta} = \frac{-i\Delta\rho}{\gamma} \quad \text{and} \quad \bar{\varphi}_a = -i\hat{V}_h(\mathbf{0})\xi_a|\lambda_a|q^{(a)}\rho_p, \quad (28)$$

where $\Delta\rho \equiv \nu_b N\rho_p + \nu_+\rho_+ + \nu_-\rho_- + \nu_w\rho_w - \rho_0$ is the deviation of the total bulk density from ρ_0 , and $q^{(a)} \equiv \sum_{\alpha=1}^N q^{(a)}_{r_\alpha}$ is the total nonelectric charge associated with the a th eigenvalue λ_a of one polymer chain. The same expressions for $\bar{\eta}$ and $\bar{\varphi}_a$ [Eq. (28)] may alternatively be obtained by requiring vanishing first functional derivatives of H with respect to $\eta(\mathbf{r})$ and $\varphi_a(\mathbf{r})$ and then seeking position-independent solutions $\eta(\mathbf{r}) \rightarrow \bar{\eta}$, $\psi(\mathbf{r}) \rightarrow \bar{\psi}$ and $\varphi_a(\mathbf{r}) \rightarrow \bar{\varphi}_a$ of the resulting $\delta H/\delta\eta(\mathbf{r}) = \delta H/\delta\psi(\mathbf{r}) = \delta H/\delta\varphi_a(\mathbf{r}) = 0$ conditions, as will be discussed below under the next subheading.

Plugging the MFT solution Eq. (28) back into Eq. (27) leads to the field Hamiltonian per unit volume $\bar{h} \equiv H/V$, given by

$$\bar{h} = \frac{\Delta\rho^2}{2\gamma} + \frac{\hat{V}_h(\mathbf{0})}{2} \left[\sum_{a=1}^{20} \lambda_a (q^{(a)})^2 \right] \rho_p^2. \quad (29)$$

In the approximate analytical approach taken in this work, we set $\eta(\mathbf{r})$ and $\varphi_a(\mathbf{r})$ to their MFT values $\bar{\eta}$ and $\bar{\varphi}_a$, while a spatially varying $\psi(\mathbf{r})$ is kept to $\mathcal{O}(\psi^2)$ in H . The field Hamiltonian in this approximation is therefore $H \approx V\bar{h} + H_{\text{RPA}}[\psi]$ where the $\mathcal{O}(\psi^2)$ terms are contained in

$$H_{\text{RPA}} = \int \frac{d\mathbf{k}}{(2\pi)^3} \frac{1}{2} \hat{\psi}(-\mathbf{k}) \left[\hat{\Gamma}^2 (N\rho_p g_{cc}(|\mathbf{k}|) + \rho_+ + \rho_-) + \frac{\mathbf{k}^2}{4\pi l_B} \right] \hat{\psi}(\mathbf{k}). \quad (30)$$

The factor $g_{cc}(k)$, given by⁹¹

$$g_{cc}(k) = \frac{1}{N} \sum_{\alpha,\beta=1}^N \sigma_\alpha \sigma_\beta e^{-|\alpha-\beta|b^2 k^2/6}, \quad (31)$$

comes from the quadratic expansion of the single polymer partition function Q_p . In our

approximation, the functional integrals in the partition function Z amounts to

$$\int \mathcal{D}\eta \int \mathcal{D}\psi \left(\prod_{a=1}^{20} \int \mathcal{D}\varphi_a \right) e^{-H[\eta, \psi, \{\varphi_a\}]} \approx e^{-V\bar{h}} \int \mathcal{D}\psi e^{-H_{\text{RPA}}} \quad (32)$$

where $V\bar{h}$ is the field Hamiltonian evaluated at homogeneous field values in accordance with Eq. (29).

To further simplify the formulation, we now take the $\gamma \rightarrow 0$ limit such that solvent density is no longer an independent component of the system but is instead determined by

$$\rho_w = \frac{1}{v_w} (\rho_0 - v_b N \rho_p - v_+ \rho_+ - v_- \rho_-). \quad (33)$$

In other words, $\Delta\rho = 0$ and, equivalently, $\rho_0 = v_b N \rho_p + v_+ \rho_+ + v_- \rho_- + v_w \rho_w$. The remaining system components $\{\rho_p, \rho_+, \rho_-\}$ are further constrained by electric charge neutrality of the system as a whole, i.e. $\sigma_p \rho_p + \rho_+ - \rho_- = 0$, where σ_p is the net electric charge of a polymer chain. To make this condition manifest, we introduce the overall salt density ρ_s , which is the overall number density of cation-anion pairs. The ion type in excess is referred to as counterions. For net-neutral or net-positive chains, $\sigma_p \geq 0$, we have $\rho_+ = \rho_s$ and $\rho_- = \sigma_p \rho_p + \rho_s$; for net-negative chains, $\sigma_p < 0$, we have $\rho_- = \rho_s$ and $\rho_+ = -\sigma_p \rho_p + \rho_s$. Taking all the above considerations together and with $k \equiv |\mathbf{k}|$, the MFT/RPA free energy per volume in units of $k_B T$, $f(\rho_p, \rho_s) \equiv -(\ln Z)/V$, becomes

$$f(\rho_p, \rho_s) = -s(\rho_p, \rho_s) - \rho_0 \chi_{\text{eff}} \phi_p^2 + \frac{1}{4\pi^2} \int_0^\infty dk k^2 \ln \left[1 + \frac{4\pi l_B}{k^2} \hat{\Gamma}^2 (2\rho_s + |\sigma_p| \rho_p + g_{cc}(k) \rho_b) \right] \quad (34)$$

after performing the $\int \mathcal{D}\psi$ integration⁹¹ in Eq. (32), wherein the term

$$-s(\rho_p, \rho_s) = \sum_{i=p,+, -, w} \rho_i \ln \rho_i \quad (35)$$

accounts for translational entropy and follows from applying Stirling's approximation $\ln n! \approx n \ln n - n$ to the factorial prefactors in Eq. (19) and neglecting terms linear in ρ_i arising from the nonlogarithmic $-n$ part of the Stirling approximation because terms linear in ρ_i in the free energy have no effect on phase separation properties.³⁸ In the second term on the right hand side of Eq. (34), $\phi_p \equiv v_b N \rho_p / \rho_0$ is the volume fraction occupied by polymer beads (and thus the volume fraction of the polymers themselves) and χ_{eff} is a dimensionless effective Flory-Huggins χ -parameter that originates from the spatially short-range interactions [cf.

second term of \bar{h} in Eq. (29)]:

$$\chi_{\text{eff}} = -\frac{\rho_0 \hat{V}_h(\mathbf{0})}{2v_b^2 N^2} \sum_{a=1}^{20} \lambda_a (q^{(a)})^2. \quad (36)$$

Using Eq. (1), the summation over a in the above expression for χ_{eff} can be reverted, i.e.,

$$\sum_{a=1}^{20} \lambda_a (q^{(a)})^2 = \sum_{\alpha=1}^N \sum_{\beta=1}^N \varepsilon_{r_\alpha, r_\beta}, \quad (37)$$

to show that it is a summation over all possible pairwise residue-residue interaction energies for a pair of heteropolymer chains with the given sequence of residues. As such, the present mean-field treatment of spatially short-range interactions is akin to the random-mixing or Bragg-Williams¹⁴⁰ approximation used in Flory-Huggins theories of proteinlike heteropolymers.^{137,141} As mentioned above, the third term in Eq. (34) corresponds to the standard RPA term accounting for Gaussian fluctuations in electric charge density. This term is obtained from functional integral over ψ in Eq. (32) followed by subtraction of the free-energy contribution at $\rho_p = \rho_s = 0$, a subtraction that has no effect on phase separation properties. Given the free energy $f(\rho_p, \rho_s)$ in Eq. (34), phase diagrams may be constructed, for example, by matching the polymer and salt chemical potentials $\mu_{p,s} = \partial f / \partial \rho_{p,s}$ and osmotic pressure $\Pi = \mu_p \rho_p + \mu_s \rho_s - f$ (ref. 78).

Field-Theoretic Simulations (FTS). One shortcoming of the above analytical approximation is that all effects of the spatially short-range interactions are condensed into the value of χ_{eff} which depends only on overall residue composition of the polymer but not the specific sequential arrangement of the residues. To tackle such sequence-specific effects, one needs to account for higher-order fluctuations in the partition function in Eq. (19). To this end, we next consider ways to study systems described by Eq. (19) using FTS because of its ability to afford, in principle, a full account of field fluctuations.¹⁴²

In FTS, each field (denoted generically as ϕ) is analytically continued into its complex plane, and approximated by a set of discrete variables defined on the sites of a cubic M^3 lattice with periodic boundary conditions and lattice spacing Δx . The fields evolve in a fictitious complex-Langevin (CL) time t according to

$$\frac{\partial \phi(\mathbf{r}, t)}{\partial t} = -\frac{\delta H}{\delta \phi(\mathbf{r}, t)} + \tilde{\eta}_\phi(\mathbf{r}, t) \quad , \quad \phi = \eta, \psi, \varphi_a, \quad (38)$$

where $\tilde{\eta}_\phi(\mathbf{r}, t)$ represents real-valued Gaussian noise with zero mean, i.e., $\langle \tilde{\eta}_\phi(\mathbf{r}, t) \tilde{\eta}_{\phi'}(\mathbf{r}', t') \rangle = 2\delta_{\phi, \phi'} \delta(t - t') \delta(\mathbf{r} - \mathbf{r}')$, where $\delta_{\phi, \phi'} = 1$ if $\phi = \phi'$ and $\delta_{\phi, \phi'} = 0$ if $\phi \neq \phi'$. Thermal averages of the real-space system can then be computed as asymptotic

CL time averages of field operators in the fictitious-time system that are constructed to correspond to the thermodynamic observable of interest.^{143,144} This approach has its origin in the development, beginning in the 1980s, of stochastic quantization¹⁴⁵ as a method for studying quantum field theories and their regularization¹⁴⁶⁻¹⁴⁸ and has since been applied extensively to study properties of polymer solutions.⁵⁸

In the present model, the functional derivatives of the field Hamiltonian H in Eq. (20) are

$$\begin{aligned}\frac{\delta H}{\delta \eta(\mathbf{r})} &= i \sum_{i=\text{b},\pm,\text{w}} v_i \tilde{\rho}_i(\mathbf{r}) - i\rho_0 + \gamma\eta(\mathbf{r}), \\ \frac{\delta H}{\delta \psi(\mathbf{r})} &= i\tilde{c}(\mathbf{r}) - \frac{\nabla^2 \psi(\mathbf{r})}{4\pi l_B}, \\ \frac{\delta H}{\delta \varphi_a(\mathbf{r})} &= i\xi_a \tilde{h}_a(\mathbf{r}) + \frac{1}{|\lambda_a|} V_h^{-1} \varphi_a(\mathbf{r}),\end{aligned}\tag{39}$$

where $\tilde{\rho}_i(\mathbf{r})$ in the first relation here in Eq. (39) is a field operator corresponding to the density of component i , and is given, respectively, by

$$\tilde{\rho}_{\pm}(\mathbf{r}) = \Gamma \star \frac{\rho_{\pm}}{Q_{\pm}} e^{-iv_{\pm}\tilde{\eta}(\mathbf{r}) \mp i\psi(\mathbf{r})} \quad \text{and} \quad \tilde{\rho}_{\text{w}}(\mathbf{r}) = \Gamma \star \frac{\rho_{\text{w}}}{Q_{\text{w}}} e^{-iv_{\text{w}}\tilde{\eta}(\mathbf{r})}\tag{40}$$

for ions and solvents, whereas the polymer bead density operator, $\tilde{\rho}_{\text{b}}(\mathbf{r})$, is computed through forward and backward chain propagators $q_{\text{F,B}}(\mathbf{r}, \alpha)$ which are constructed by applying the following relations iteratively:^{62,78,91}

$$\begin{aligned}q_{\text{F}}(\mathbf{r}, \alpha + 1) &= e^{-W_{\alpha+1}(\mathbf{r})} \Phi \star q_{\text{F}}(\mathbf{r}, \alpha), \\ q_{\text{B}}(\mathbf{r}, \alpha - 1) &= e^{-W_{\alpha-1}(\mathbf{r})} \Phi \star q_{\text{B}}(\mathbf{r}, \alpha),\end{aligned}\tag{41}$$

where $\Phi(\mathbf{r}) = e^{-3\mathbf{r}^2/2b^2} / (2\pi b^2/3)^{3/2}$, and initiating from $q_{\text{F}}(\mathbf{r}, 1) = e^{-W_1(\mathbf{r})}$ and $q_{\text{B}}(\mathbf{r}, N) = e^{-W_N(\mathbf{r})}$. Given $q_{\text{F,B}}$, the polymer bead density operator can be computed as

$$\tilde{\rho}_{\text{b}}(\mathbf{r}) = \Gamma \star \frac{\rho_{\text{p}}}{Q_{\text{p}}} \sum_{\alpha=1}^N e^{W_{\alpha}(\mathbf{r})} q_{\text{F}}(\mathbf{r}, \alpha) q_{\text{B}}(\mathbf{r}, \alpha),\tag{42}$$

with

$$Q_{\text{p}} = \frac{1}{V} \int d\mathbf{r} q_{\text{F}}(\mathbf{r}, N).\tag{43}$$

In the second relation in Eq. (39), $\tilde{c}(\mathbf{r}) = \tilde{c}_{\text{b}}(\mathbf{r}) + \tilde{\rho}_{+}(\mathbf{r}) - \tilde{\rho}_{-}(\mathbf{r})$ is a field operator corresponding to the electric charge density, wherein the polymer bead contribution $\tilde{c}_{\text{b}}(\mathbf{r})$ is given by

$$\tilde{c}_{\text{b}}(\mathbf{r}) = \Gamma \star \frac{\rho_{\text{p}}}{Q_{\text{p}}} \sum_{\alpha=1}^N e^{W_{\alpha}(\mathbf{r})} q_{\text{F}}(\mathbf{r}, \alpha) q_{\text{B}}(\mathbf{r}, \alpha) \sigma_{\alpha}.\tag{44}$$

In the third relation in Eq. (39), the field operators for the nonelectric charge densities associated with the spatially short-range interactions, $\tilde{h}_a(\mathbf{r})$, are similarly given by

$$\tilde{h}_a(\mathbf{r}) = \Gamma \star \frac{\rho_p}{Q_p} \sum_{\alpha=1}^N e^{W_\alpha(\mathbf{r})} q_F(\mathbf{r}, \alpha) q_B(\mathbf{r}, \alpha) q^{(a)}_{r_\alpha}. \quad (45)$$

It can be readily verified that the position-independent solution to $\delta H/\delta\phi(\mathbf{r}) = 0$ for $\phi = \eta, \psi, \varphi_a$ (where the expressions for the functional derivatives are given in Eq. (39)) yields exactly the MFT solution in Eq. (28) for position-independent η and φ_a (together with any value of position-independent ψ): For any set of values of the position-independent fields, the field operators for number and charge densities become equal to their bulk counterparts, i.e. $\tilde{\rho}_{b,\pm,w}(\mathbf{r}) = \rho_{b,\pm,w}$, $\tilde{c}(\mathbf{r}) = \rho_p\sigma_p + \rho_+ - \rho_- = 0$ and $\tilde{h}_a(\mathbf{r}) = \rho_p q^{(a)}$. Substituting this into Eq. (39) and setting the functional derivatives to zero gives exactly the expressions in Eq. (28).

In contrast to the approximate analytical approach introduced under the previous sub-heading, FTS depends on the full analytical form of the spatially short-range interaction potential $V_h(r)$, where $r = |\mathbf{r}|$, not only its spatial integral $\int d\mathbf{r} V_h(r) = \hat{V}_h(\mathbf{0})$ that appears as part of an effective Flory-Huggins χ -parameter, χ_{eff} , in Eq. (36). Several functional forms for spatially short-range interactions have been used extensively in recent coarse-grained simulations of IDP LLPS.^{40,43,117} These include the common Lennard-Jones (LJ) potential

$$V_{\text{LJ}}(\mathcal{E}, \sigma|r) = 4\mathcal{E} \left[\left(\frac{\sigma}{r}\right)^{12} - \left(\frac{\sigma}{r}\right)^6 \right], \quad (46)$$

where \mathcal{E} is the depth of the potential well and σ is a length scale, and LJ variations such as the shifted Weeks–Chandler–Andersen (WCA) potential¹⁴⁹ for finite-range purely repulsive interactions as well as the recently proposed Wang-Frenkel potential¹⁵⁰ with a finite spatial range r_c ,

$$V_{\text{WF}}(\mathcal{E}, \mu, \nu, r_c, \sigma|r) = \mathcal{E} \alpha_{\text{WF}}(\mu, \nu, r_c, \sigma) \left[\left(\frac{\sigma}{r}\right)^{2\mu} - 1 \right] \left[\left(\frac{r_c}{r}\right)^{2\mu} - 1 \right]^{2\nu} \quad (47)$$

for $r \leq r_c$ and $V_{\text{WF}}(\mu, \nu, r_c, \sigma|r) = 0$ for $r > r_c$ with

$$\alpha_{\text{WF}}(\mu, \nu, r_c, \sigma) = 2\nu \left(\frac{r_c}{\sigma}\right)^{2\mu} \left\{ \frac{1 + 2\nu}{2\nu[(r_c/\sigma)^{2\mu} - 1]} \right\}^{2\nu+1}, \quad (48)$$

that enjoys several apparent numerical advantages when applied to many-body simulations, including its smooth decay to zero as r is increased toward the cutoff distance r_c . Note that the original notation in ref. 150 for the Wang-Frenkel form is largely followed in Eqs. (47) and (48). The symbols α_{WF} and μ here should not be confused with the polymer bead label

$\alpha = 1, 2, \dots, N$ and the symbol for chemical potential. The length scale σ in Eqs. (46)–(48) also should not be confused with the symbol for electric charge defined above in our formulation.

Mathematically, however, these potential functions cannot practically—if at all possibly—be incorporated into our field-theoretic formalism because the field Hamiltonian H in Eq. (20) requires the inverse operator, V_h^{-1} , of the potential function but no inverse operator expressed in terms of elementary functions is known for V_{LJ} and V_{WF} . (For a recent promising approach for including general pairwise interaction potentials in FTS, see ref. 151). This consideration leads us to the Yukawa potential,¹⁵² which has the same mathematical form as the screened Coulomb potential, because it possesses an inverse expressible in terms of Fourier transform of elementary functions. Therefore, as a first step in the exploration of our general theoretical framework, we specialize here to a Yukawa form for the spatially short-range interactions, viz.,

$$V_h(r) = \frac{l_h e^{-\kappa r}}{r}, \quad (49)$$

where interaction strength is represented by l_h and the spatial range of the interaction is characterized by the reciprocal κ^{-1} of the screening coefficient κ (Fig. 4). The Fourier transform of $V_h(r)$ is given by $\hat{V}_h(\mathbf{k}) = \hat{V}_h(k) = 4\pi l_h / (k^2 + \kappa^2)$, and the inverse of $V_h(r)$ as defined by Eq. (25) is $V_h^{-1} = (-\nabla^2 + \kappa^2) / 4\pi l_h$. In view of the MFT result in Eq. (36), the overall spatial range-dependent interaction strength of the Yukawa potential may also be quantified by $\hat{V}_h(\mathbf{0}) = 4\pi l_h / \kappa^2$.

Pair Correlation Functions. Structural information of the molecular species in our model system can be inferred from pair correlation functions,^{62,92} defined here as

$$G_{p,q}(|\mathbf{r} - \mathbf{r}'|) = \langle \hat{\rho}_p(\mathbf{r}) \hat{\rho}_q(\mathbf{r}') \rangle - \delta_{pq} \rho_q \frac{e^{-|\mathbf{r} - \mathbf{r}'|^2 / 4a_s^2}}{(4\pi a_s^2)^{3/2}}, \quad p, q = \text{b}, \pm, \text{w}, \quad (50)$$

where the second term on the right hand side of the equation for $G_{p,q}$ subtracts the trivial correlation of a particle with itself. Correlation functions were used to quantify the degree of condensed-state subcompartmentalization of phase-separated polyampholytes in FTS and coarse-grained explicit-chain models⁶² and have been applied more recently to analyze experimental data on the biomolecular structure of nucleolar condensates.¹⁵³ The pair correlation functions are, in turn, related to the potentials of mean force (PMFs), $U_{p,q}(r)$, through the standard formula

$$U_{p,q}(r) = -k_B T \ln \left[\frac{G_{p,q}(r)}{\rho_p \rho_q} \right], \quad (51)$$

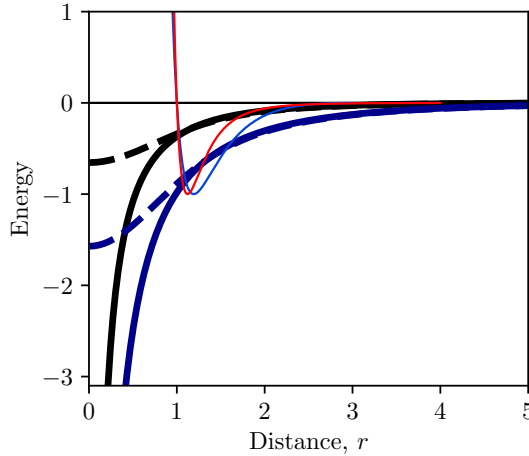


Fig. 4: The Yukawa potential as a model of spatially short-range favorable interactions. Two examples of $V_h(r)$ in Eq. (49) are depicted by the thick solid black curve ($l_h = 6\sigma/3.8$, $\kappa = 3.8/8\sigma$) and the thick solid blue curve ($l_h = 3\sigma/3.8$, $\kappa = 3.8/5\sigma$) with $\sigma = 1$; i.e., σ is the unit for r in this plot. The dashed curves (same color code) provide the corresponding “smeared” version of these potentials defined as $(1/2\pi^2) \int_0^\infty dk k^2 \hat{\Gamma}(k)^2 \hat{V}(k) \sin(kr)/kr$ where $\hat{\Gamma}(k) = \exp(-a_s^2 k^2/2)$ is the Fourier transform of the function $\Gamma(\mathbf{r})$ in Eq. (11) with $a_s = \sigma/\sqrt{6}$ shown as an example here. The interaction between two point particles via this smeared Yukawa potential is mathematically equivalent to that between two particles modeled as Gaussian distributions $\Gamma(\mathbf{r})$ via the original $V_h(r)$. Included for comparison are a LJ potential (red curve, Eq. (46) with $\mathcal{E} = 1$) and a Wang-Frenkel potential (thin blue curve, Eq. (47) with $\mathcal{E} = 1$, $\mu = \nu = 1$, and $r_c = 3\sigma$). The example Yukawa potentials are selected to match approximately with either the potential wells (thick blue curves) or the large- r trends (thick black curves) of the LJ and Wang-Frenkel potentials.

where the normalization factor $\rho_p \rho_q$ in the argument of the logarithm is chosen such that $U_{p,q} < 0$ means correlation and $U_{p,q} > 0$ implies anti-correlation. In FTS, the pair correlation functions can be computed using the following relations:

$$\begin{aligned} \langle \hat{\rho}_p(\mathbf{r}) \hat{\rho}_q(\mathbf{r}') \rangle &= \langle \tilde{\rho}_p(\mathbf{r}) \tilde{\rho}_q(\mathbf{r}') \rangle \quad , \quad (p \neq q), \\ \langle \hat{\rho}_p(\mathbf{r}) \hat{\rho}_p(\mathbf{r}') \rangle &= \left\langle \frac{\tilde{\rho}_p(\mathbf{r})}{v_p} \left(\frac{i}{\gamma} \eta(\mathbf{r}') + \rho_0 - \sum_{q \neq p} v_q \tilde{\rho}_q(\mathbf{r}') \right) \right\rangle . \end{aligned} \quad (52)$$

In accordance with a common procedure in field theory,¹⁵⁴ these relations can be derived by adding source terms $\sum_p \int d\mathbf{r} \hat{\rho}_p(\mathbf{r}) J_p(\mathbf{r})$ to the particle Hamiltonian \hat{H} in Eq. (7) and then taking functional derivatives with respect to $J_p(\mathbf{r})$ s in the resulting field theory and finally setting all $J_p \rightarrow 0$. The formula for the self-correlation function $\langle \hat{\rho}_p \hat{\rho}_p \rangle$ may be obtained⁶² through an intermediate field re-definition to avoid a term that contains a double derivative of Q_p .

Coarse-Grained Explicit-Chain Models. Following our previous studies,^{62,66,91}

coarse-grained explicit-chain molecular dynamics (MD) simulations are conducted here to elucidate the ramifications of several proposed interaction schemes^{40,66,111,112,116,117} and to assess the accuracy of our approximate analytical theories and FTS in capturing the essential physics of biomolecular LLPS. As before,^{40,43} each amino acid is represented by a single bead of different mass and size. Although it is possible to incorporate explicit simple dipole solvent molecules in coarse-grained explicit-chain LLPS simulation to better account for dielectric effects,⁹¹ for simplicity we will limit the present study to implicit-solvent simulations.^{40,66} As the general features of the model can be found in the literature,^{40,66,111,112,116,117} only an outline is provided here. Briefly, as in the above field-theory formulation, let n_p be the total number of N -residue polypeptide chains (IDPs) in the MD system, with the chains labeled by i or $j = 1, 2, \dots, n_p$ and the residues (beads) along a polypeptide chain labeled by α or $\beta = 1, 2, \dots, N$. The total potential energy U_T is a function of the residue positions $\{\mathbf{R}_{i,\alpha}\}$ that may be written as

$$U_T = U_{\text{bond}} + U_{\text{el}} + U_{\text{hh}} , \quad (53)$$

where U_{bond} is the bond-length term for chain connectivity:

$$U_{\text{bond}} = \frac{K_{\text{bond}}}{2} \sum_{i=1}^{n_p} \sum_{\alpha=1}^{N-1} (R_{i,\alpha+1;i,\alpha} - l)^2 \quad (54)$$

with $R_{i,\alpha;j,\beta} \equiv |\mathbf{R}_{i,\alpha} - \mathbf{R}_{j,\beta}|$. Parameter values for the MD potential U_{bond} in Eq. (54) and for U_{el} , U_{hh} below are different across the three interaction schemes—Mpipi,¹¹⁷ Urry,¹¹¹ and FB¹¹²—that we apply here to the Ddx4 IDRs.⁶⁶ To facilitate comparisons with prior coarse-grained MD simulation results in the literature, the parameters in these original references are largely used with the corresponding interaction schemes in the present simulations unless stated otherwise. For U_{bond} , $K_{\text{bond}} = 19.1917 \text{ kcal mol}^{-1} \text{ \AA}^{-2}$, $l = 3.81 \text{ \AA}$ for Mpipi;¹¹⁷ $K_{\text{bond}} = 9.56 \text{ kcal mol}^{-1} \text{ \AA}^{-2}$, $l = 3.82 \text{ \AA}$ for Urry;¹¹¹ and $K_{\text{bond}} = 2.39 \text{ kcal mol}^{-1} \text{ \AA}^{-2}$, $l = 3.8 \text{ \AA}$ for FB.¹¹² The U_{el} term in Eq. (53) is the electrostatic interaction:

$$U_{\text{el}} = \sum_{i,j=1}^{n_p} \sum_{\substack{\alpha,\beta=1 \\ (i,\alpha) \neq (j,\beta)}}^N \frac{\sigma_{i,\alpha} \sigma_{j,\beta} e^2}{4\pi\epsilon_0\epsilon_r R_{i,\alpha;j,\beta}} \exp\left(-\kappa_D R_{i,\alpha;j,\beta}\right) , \quad (55)$$

where, as in Eq. (13), $\sigma_{i,\alpha}$ is the electric charge, in units of proton charge e , of the α th residue along the i th chain (as stated above for the field-theoretic formulation, $\sigma_{i,\alpha} = \sigma_\alpha$ is independent of i in the present MD simulations), and κ_D is the reciprocal of the Debye screening length. Mpipi¹¹⁷ uses $\sigma_\alpha = +0.75$ for the positively charged residues arginine and lysine, $\sigma_\alpha = +0.375$ for histidine (to account for its incomplete ionization under physiological conditions), and $\sigma_\alpha = -0.75$ for the negatively charged residues aspartic and glutamic acids; Urry¹¹¹ uses $\sigma_\alpha = +1$ for arginine and lysine, $\sigma_\alpha = 0$ for histidine, and $\sigma_\alpha = -1$ for aspartic

and glutamic acids; and FB¹¹² uses $\sigma_\alpha = +1$ for arginine and lysine, $\sigma_\alpha = +0.5$ for histidine, and $\sigma_\alpha = -1$ for aspartic and glutamic acids. All other residues have $\sigma_\alpha = 0$ in all of these three interaction schemes. In all of the present coarse-grained MD simulations, we set $\kappa_D = 0.1 \text{ \AA}^{-1}$ (i.e., a Debye screening length of 10 \AA corresponding to a physiological monovalent salt concentration of $\sim 100 \text{ mM}$), apply a large-distance cutoff of 35 \AA to the electrostatic interaction, and use a dielectric constant $\epsilon_r = 40$. Employing a dielectric constant moderately lower than the $\epsilon_r \approx 80$ value of bulk water in coarse-grained MD simulation of IDP LLPS has recently been rationalized from a theoretical perspective^{66,91} and this modeling practice is apparently not inconsistent with experimental observations of slower water orientational dynamics in living matter.¹⁵⁵

For the spatially short-range interaction term U_{hh} in Eq. (53), Mpipi¹¹⁷ uses the Wang-Frenkel form,¹⁵⁰ viz.,

$$U_{\text{hh}}^{\text{Mpipi}} = \sum_{\substack{i,j=1 \\ (i,\alpha) \neq (j,\beta)}}^{n_p} \sum_{\substack{\alpha,\beta=1 \\ N}}^N V_{\text{WF}}(\mathcal{E}_{\alpha,\beta}, \mu_{\alpha,\beta}, 1, (r_c)_{\alpha,\beta}, \sigma_{\alpha,\beta} | R_{i,\alpha;j,\beta}), \quad (56)$$

where, by definition, $V_{\text{WF}}(\mathcal{E}_{\alpha,\beta}, \mu_{\alpha,\beta}, 1, (r_c)_{\alpha,\beta}, \sigma_{\alpha,\beta} | R_{i,\alpha;j,\beta})$ vanishes for $R_{i,\alpha;j,\beta} > (r_c)_{\alpha,\beta}$ as specified in Eqs. (47) and (48). For all amino acid residue pairs α, β , Mpipi sets the distance cutoff $(r_c)_{\alpha,\beta} = 3\sigma_{\alpha,\beta}$ and assigns $\nu = 1$. Values of the interaction strength $\mathcal{E}_{\alpha,\beta}$, length scale $\sigma_{\alpha,\beta}$, and the parameter $\mu_{\alpha,\beta}$ for the Wang-Frenkel functional form depend on the amino acid residue types r_α and r_β for residues α and β . The Mpipi values for $\mathcal{E}_{r,r'}$, $\sigma_{r,r'}$, and $\mu_{r,r'}$, where r and r' each represents one of the twenty amino acid types, are provided in Supplementary Table 11 of ref. 117, wherein $\mu_{r,r'} = 2$ for almost all pairs of residue types except for a few cases in which $\mu_{r,r'} = 4$ or 11.

For the Urry¹¹¹ and FB¹¹² interaction schemes, U_{hh} in Eq. (53) is given by⁴⁰

$$U_{\text{hh}}^{\text{Urry/FB}} = \sum_{\substack{i,j=1 \\ (i,\alpha) \neq (j,\beta)}}^{n_p} \sum_{\substack{\alpha,\beta=1 \\ N}}^N (U_{\text{hh}})_{i,\alpha;j,\beta}^{\text{Urry/FB}} \quad (57)$$

where

$$(U_{\text{hh}})_{i,\alpha;j,\beta}^{\text{Urry/FB}} = \begin{cases} V_{\text{LJ}}(\mathcal{E}_{\alpha,\beta}, \sigma_{\alpha,\beta} | R_{i,\alpha;j,\beta}) + (1 - \lambda_{\alpha,\beta}^{\text{hh}}) \mathcal{E}_{\alpha,\beta} & \text{if } R_{i,\alpha;j,\beta} \leq 2^{1/6} \sigma_{\alpha,\beta} \\ \lambda_{\alpha,\beta}^{\text{hh}} V_{\text{LJ}}(\mathcal{E}_{\alpha,\beta}, \sigma_{\alpha,\beta} | R_{i,\alpha;j,\beta}) & \text{otherwise} \end{cases} \quad (58)$$

is in the Ashbaugh-Hatch form¹⁵⁶ with the function V_{LJ} given by Eq. (46). For both Urry and FB, $\mathcal{E}_{\alpha,\beta} = \mathcal{E} = 0.2 \text{ kcal mol}^{-1}$ irrespective of the residue types r_α, r_β of residues α, β , and the length scale $\sigma_{\alpha,\beta} = [\sigma(r_\alpha) + \sigma(r_\beta)]/2$, where $\sigma(r_\alpha)$ is the diameter of the bead model for amino acid residue type r_α given by the quantity σ in Table S1 of ref. 40. In both

interaction schemes, $\lambda_{\alpha,\beta}^{\text{hh}} = [\lambda(r_\alpha) + \lambda(r_\beta)]/2$, where $\lambda(r_\alpha)$ is the hydrophobicity/hydropathy parameter for residue type r_α . The $\lambda(r_\alpha)$ values for the Urry interaction scheme are given by the ‘‘Urry et al. normalized hydropathy scale’’ column of Table S2 in ref. 111, whereas the corresponding $\lambda(r_\alpha)$ values for the FB interaction scheme are provided in Table S7 of ref. 112. In simulations that use the Urry and FB interaction schemes, a cutoff distance of 20 Å is applied to the $(U_{\text{hh}})_{i,\alpha;j,\beta}^{\text{Urry/FB}}$ interactions in Eq. (58).

In addition to modeling Ddx4 IDRs, to investigate nonelectrostatic effects of sequence pattern on LLPS, coarse-grained explicit-chain MD simulations are also conducted here for copolymer sequences consisting of only two types of residues, both with zero electric charge, but possess different hydrophobicities. The hydrophobic-polar patterns of these model sequences—commonly referred to as HP sequences in the protein literature^{61,141,157,158}—are taken from recent studies of their LLPS.^{132,133} In keeping with tradition of surfactant models, however, hydrophobic and polar beads were labeled, respectively, as ‘‘T’’ (tail) and ‘‘H’’ (head) in refs. 132, 133. Here we use leucine for the hydrophobic beads and serine for the polar beads. The resulting amino acid sequences are thus referred to as LS sequences. As a test case, we use the KH interaction scheme⁴⁰ described in ref. 66 for the present LS-sequence simulations. Specifically, the spatially short-range interaction U_{hh} is in the form of Eqs. (57) and (58) wherein $\mathcal{E}_{\alpha,\beta} = 0.228|(e_{\text{MJ}})_{r_\alpha,r_\beta} - e_0|$, $\lambda_{\alpha,\beta}^{\text{hh}} = 1$ if $(e_{\text{MJ}})_{r_\alpha,r_\beta} \leq e_0$ and $\lambda_{\alpha,\beta}^{\text{hh}} = -1$ otherwise, $e_0 = -1.0 \text{ kcal mol}^{-1}$ and $(e_{\text{MJ}})_{r_\alpha,r_\beta}$ is from ref. 115. The KH-D parameter set in Table S3 of ref. 40 corresponds to $-\lambda_{\alpha,\beta}^{\text{hh}}\mathcal{E}_{r_\alpha,r_\beta}$.

MD Simulation of LLPS. Based on the models described above, we follow the recently developed, widely-applied slab method for simulation of IDP LLPS.^{40,43,78} Because this simulation protocol, its rationale, and the procedure to construct phase diagrams from equilibrated simulations have been detailed elsewhere,^{40,43,67} a brief outline here will suffice. As in our previous studies,^{43,62,66,78,91} the GPU version of HOOMD-Blue software^{159,160} is employed in the present simulations. For each simulation of the wildtype or a variant of the 236-residue Ddx4 IDR,⁶⁶ 100 chains are randomly placed in a sufficiently large cubic box of dimension $300 \times 300 \times 300 \text{ Å}^3$ initially. Energy minimization is then performed to remove any steric clashes among the model molecules. This is followed by *NPT* compression at a temperature of 100 K and pressure of 1 atm for a period of 50 ns using the Martyna-Tobias-Klein (MTK) thermostat and barostat^{161,162} with a coupling constant of 1 ps. The equations of motion are integrated with velocity-Verlet algorithm using a large timestep of 10 fs. Periodic boundary conditions are applied in all three directions. The electrostatic interaction is treated with the PPPM algorithm.¹⁶³ After the initial *NPT* compression, the system is compressed again at 100 K for a period of 50 ns using Langevin thermostat with a friction coefficient of 1 ps^{-1} to reach a sufficiently high density phase of IDPs enclosing in a simulation box of size $150 \times 150 \times 150 \text{ Å}^3$. At this point, the system

is expanded along one of the axes (referred to as the z -axis) to 3000 Å for 10 ns with the temperature fixed at 100 K. Next, an NVT equilibration is performed for 2 μ s at desired temperatures using the Langevin thermostat with a friction coefficient of 1 ps⁻¹. Final production run is then carried out for another 4 μ s with the same Langevin thermostat using a lower friction coefficient of 0.01 ps⁻¹. Snapshots are saved every 1 ns for analysis. A similar procedure is used for the simulations of the 20-residue leucine-serine sequences LS1, LS2, and LS3. Here, the only difference with the Ddx4 IDR simulations is that 1,000 LS chains are used for each simulation and the simulation box is compressed to a size of $130 \times 130 \times 130$ Å³ and then expanded to 2000 Å along the z -axis. Details regarding how to construct phase diagrams from equilibrium trajectories are described in refs. 40, 43, 66, 78.

RESULTS AND DISCUSSION

While we consider the above-detailed theoretical development to be the main thrust of this article and that extensive testing of our theory is beyond the scope of the present work, it is instructive to apply the new formulation to a few initial examples to probe our theory’s practical effectiveness and to provide suggestions for future theoretical/computational improvements based upon the success and limitation of the following examinations. We do so by using our formulation on four well-studied Ddx4 IDRs^{9,19,66,98,111,117} as well as three selected hydrophobic-polar model sequences that have the same composition but different hydrophobic/polar sequence patterns.¹³²

Analytical Theory for the Phase Behaviors of Wildtype and Variant Ddx4 IDRs Modeled by Different Interaction Schemes. To illustrate the approximate analytical approach in the previous section, we apply the theory with the free energy function given by Eq. (34) to the 236-residue wildtype (WT), charge-scrambled (CS), arginine-to-lysine (RtoK), and phenylalanine-to-alanine (FtoA) variants of the Ddx4 IDR (the amino acid sequences are provided, for example, in Fig. S1 of ref. 66). We compare the LLPS properties predicted by using $\varepsilon_{r,r'}$ s from the five interaction schemes illustrated in Fig. 2. In accordance with Eqs. (36) and (37) for χ_{eff} , all nonzero eigenvalues λ_a s are included in the application of the MFT/RPA Eq. (34) to the four Ddx4 IDRs.

Fig. 5 shows the nonelectric charge profiles of the WT, RtoK and FtoA Ddx4 IDRs for the two most dominant eigenvalues $\lambda_{1,2}$ in each of the five interaction schemes considered. Significant differences in nonelectric charge profiles are observed across different interaction schemes (Fig. 5a–e), reflecting variations in the assumptions made by KH, Mpipi, HPS, Urry, and FB regarding physical driving forces in biomolecular processes. Variation in the two dominant nonelectric charges along the IDR sequences (as function of the horizontal

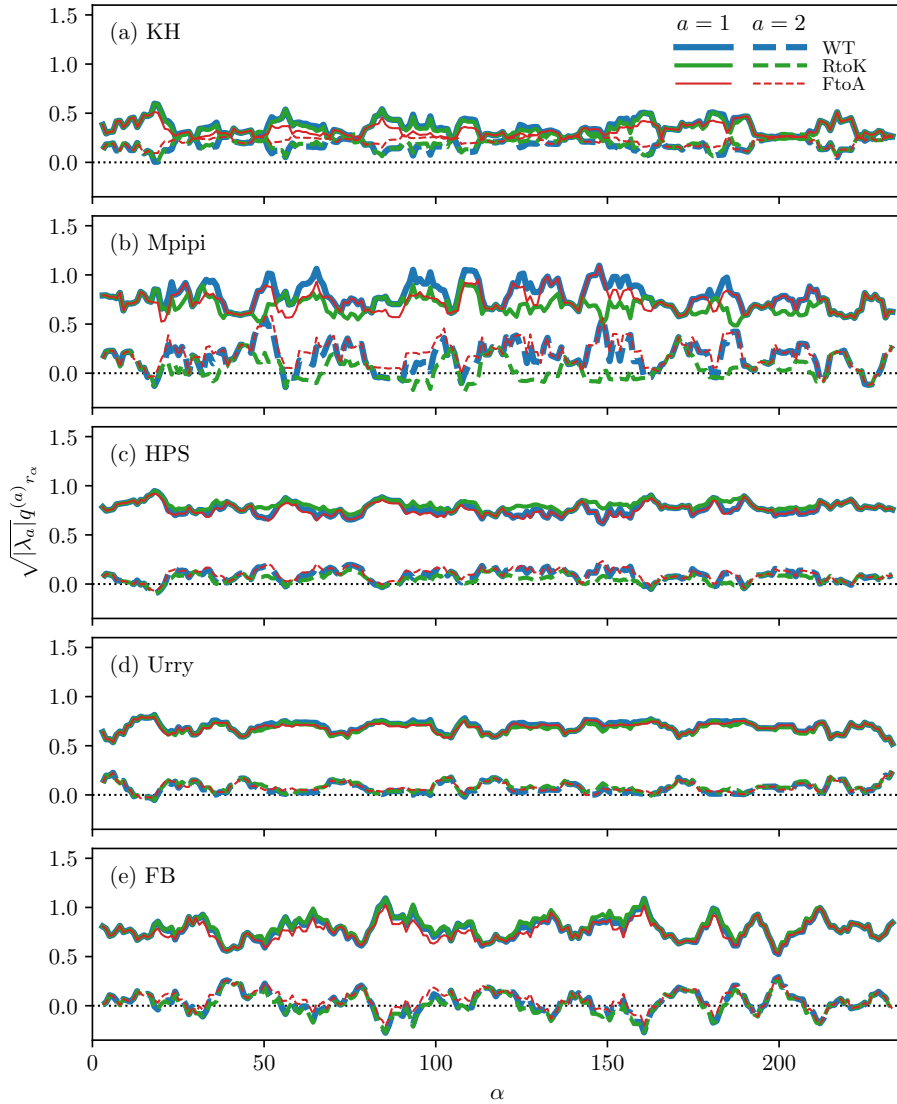


Fig. 5: Nonelectric charge profiles for Ddx4 IDRs. Distributions of nonelectric charges $q^{(a)}_{r_\alpha}$ for the two most dominant eigenvalues $a = 1, 2$ of $\varepsilon_{r,r'}$ [Eq. (1)] along the WT, RtoK and FtoA Ddx4 sequences are shown in the (a) KH, (b) Mpipi, (c) HPS, (d) Urry, and (e) FB interaction schemes [key for line styles provided in (a)]. The nonelectric charge profiles in this figure are averages of individual residues' $q^{(1)}_{r_\alpha}$ or $q^{(2)}_{r_\alpha}$ over a sliding window of six residues. As generally defined in the text, $\alpha = 1, 2, \dots, 236$ is the sequential position label of the residues along the Ddx4 IDRs, and r_α is the amino acid type of residue α .

variable α) is discernibly more pronounced in Mpipi and FB than in HPS and Urry, with KH exhibiting an intermediate degree for variation along the chain sequence. Implications of this difference for predicted LLPS propensity remain to be ascertained. Within the same interaction scheme, the variation in nonelectric charge profiles among the three Ddx4 sequence variants (shown by curves in different colors in Fig. 5) is notably higher for the KH and Mpipi interaction schemes with 210 contact energies than for the HPS, Urry, and

FB interaction schemes that are based upon 20-value hydrophobicity/hydropathy scales, indicating that the LLPS propensities of the sequence variants predicted by KH and Mpipi may be more diverse in KH and Mpipi than those predicted by HPS, Urry, and FB.

Because the WT, RtoK and FtoA Ddx4 IDRs share the same sequence electric charge pattern, any sequence dependence of LLPS propensity among these three sequences in the MFT/RPA analytical approach originates from the difference in their χ_{eff} parameters, which may be computed from the eigenvalues λ_a of the spectral decomposition of $\varepsilon_{r,r'}$ in conjunction with the nonelectric charges $q^{(a)}_{r\alpha}$ using Eq. (36) or directly from the interaction matrix $\varepsilon_{r,r'}$ itself via the identity in Eq. (37). In the present MFT/RPA formulation, which for simplicity assigns the same $V_h(r)$ to every residue-residue interaction scheme considered, the ratios between these χ_{eff} parameters depend only on $\varepsilon_{r,r'}$ but not $V_h(r)$. As such, these ratios may serve as a zeroth order approximate measure of the relative contributions to LLPS propensity from the spatially short-range, nonelectrostatic interactions encoded by the different IDR sequences. Accordingly, for the five interaction schemes we consider, the relative short-spatial-range interaction strengths among the WT, CS, RtoK and FtoA Ddx4 IDRs is quantified by MFT in terms of the ratios

$$\chi_{\text{eff}}^{(\text{WT,CS})} : \chi_{\text{eff}}^{(\text{RtoK})} : \chi_{\text{eff}}^{(\text{FtoA})} \quad (59)$$

wherein WT and CS share the same χ_{eff} because the WT and CS sequences have the same amino acid composition. Utilizing the $\varepsilon_{r,r'}$ values of the interaction schemes^{40,111,112,117} in Eqs. (36) and (37) leads to the following ratio:

$$\begin{aligned} \chi_{\text{eff}}^{(\text{WT,CS})} : \chi_{\text{eff}}^{(\text{RtoK})} : \chi_{\text{eff}}^{(\text{FtoA})} \\ 1 : 0.83 : 0.66 \quad (\text{KH}) \\ 1 : 0.80 : 0.84 \quad (\text{Mpipi}) \\ 1 : 1.09 : 0.97 \quad (\text{HPS}) \\ 1 : 0.96 : 0.97 \quad (\text{Urry}) \\ 1 : 1.04 : 0.94 \quad (\text{FB}) . \end{aligned} \quad (60)$$

Phase diagrams can readily be constructed⁷⁸ using the MFT/RPA free energy function in Eq. (34). To facilitate comparison of the five different interaction schemes, the overall strength of the spatially short-range interactions, encapsulated by $\hat{V}_h(\mathbf{0})$, is adjusted for each interaction scheme separately such that $\chi_{\text{eff}}^{(\text{WT,CS})} = 0.5$ at a reference temperature of $T = 300$ K. We also set $l_B = 7 \text{ \AA}$ at the same reference temperature throughout, and assume the temperature dependence of l_B , $\hat{V}_h(\mathbf{0}) \propto T^{-1}$ (as stated above, $V_h(r)$ is potential energy in units of $k_B T$). Other parameters used are $v_w = 1$, $v_b = 2$, $v_{\pm} = 0$, $a_s = b/\sqrt{6}$, and $\rho_0 = 55.5$ M. In our MFT/RPA calculations for all the interaction schemes considered

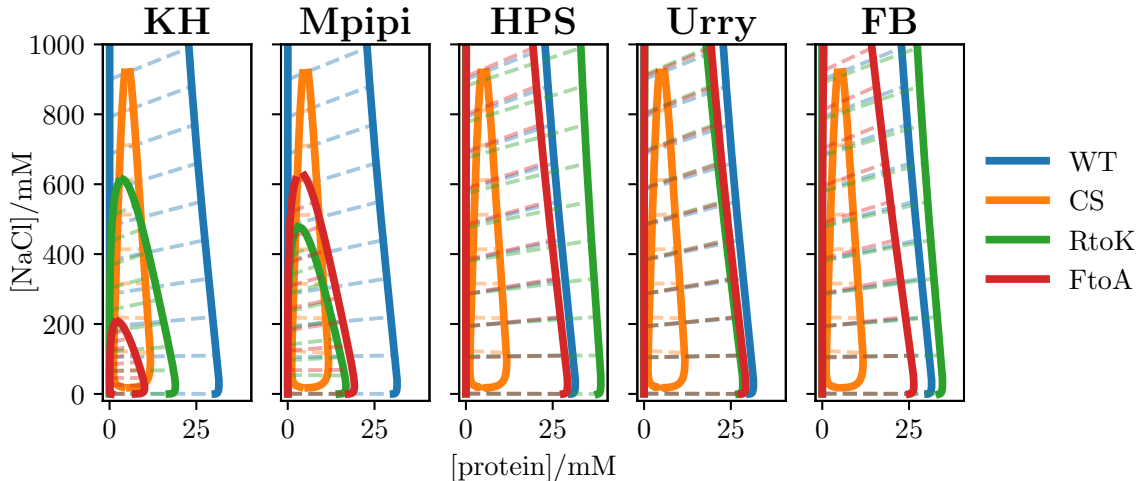


Fig. 6: Salt-dependent phase behaviors of Ddx4 IDRs computed by analytical theory. Phase diagrams of the four Ddx4 variants (color-coded on the right) on the protein-salt density (ρ_p, ρ_s) plane are computed in our approximate MFT/RPA analytical approach [Eq. (34)] at model temperature $T = 280$ K using five different interaction schemes as indicated by the top labels. The phase-separated regimes are enclosed by coexistence (binodal) curves (solid curves), (ρ_p, ρ_s) of coexisting phases are connected by tie-lines (dashed lines with the same color code for the sequence variants). All parameter values used for this figure are described in the text.

here, electric charge is $+e$ for residues R and K, $-e$ for D and E, and zero for all the other residues.

Fig. 6 shows phase diagrams in the (ρ_p, ρ_s) plane, where the two-phase region is enclosed by the coexisting (binodal) curves (solid lines). Systems with bulk concentrations within the two-phase region separate into two phases with the partition of molecular species provided by the tie-lines (dashed lines in Fig. 6). The phase diagrams in Fig. 6 are computed at a uniform temperature of $T = 280$ K, which is chosen to be sufficiently low such that every Ddx4 IDR phase separates under any one of the spatially short-range interaction scheme we consider.

Fig. 7 shows (ρ_p, T) phase diagrams of the same systems at a constant bulk protein density of $\rho_p = 10$ mM (indicated by the vertical grey dashed lines), and at two bulk salt densities $\rho_s = 100$ mM (top) and 300 mM (bottom). The phase diagrams were constructed by first computing constant-temperature binodal curves (such as Fig. 6) in the range $150 \text{ K} \leq T \leq 510 \text{ K}$. At each temperature, we check if the point (ρ_p, ρ_s) lies in the two-phase region and then identify the tie-line it intersects. The densities of the coexisting phases are then given by the two points on the binodal curve connected by the tie-line. It should be noted however that, by construction, the coexisting protein densities provided by Fig. 7 for a given temperature and a given bulk salt concentration apply only to systems with bulk protein density $\rho_p = 10$ mM. The coexisting protein densities (i.e., the phase dia-

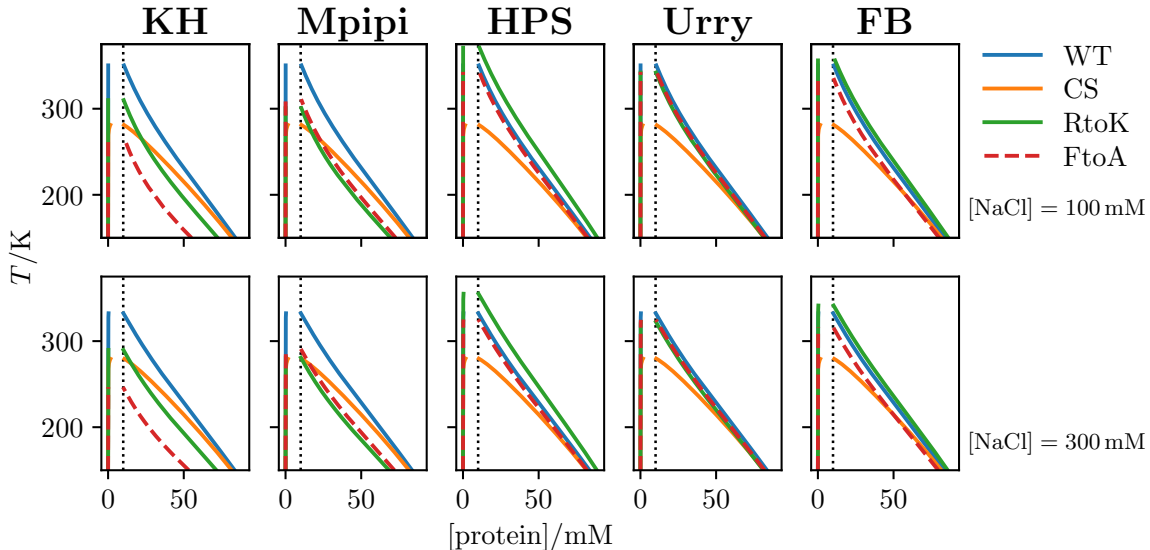


Fig. 7: Temperature-dependent phase behaviors of Ddx4 IDRs computed by analytical theory. As in Fig. 6, phase diagrams are computed in our approximate MFT/RPA analytical approach [Eq. (34)] using five different interaction schemes. Shown here are protein density (ρ_p) versus model temperature (T) phase diagrams for overall (bulk) monovalent salt ($[\text{NaCl}]$) concentrations of 100 mM (top row) and 300 mM (bottom row). These are constructed using constant- T (ρ_p, ρ_s) phase diagrams (exemplified by Fig. 6) at multiple T . For a given T , the two coexisting ρ_p s at bulk salt density $\rho_s = 100$ or 300 mM are obtained as the ρ_p values at the two ends of a (ρ_p, ρ_s) coexistence tie-line that passes through the intersection point of $\rho_p = 10$ mM (indicated by the vertical dotted lines in the present figure) and $\rho_s = 100$ mM or $\rho_s = 300$ mM, respectively, in the ρ_p - ρ_s plane. The color code for the Ddx4 variants are the same as that in Fig. 6. Dashed curves are used here for FtoA to facilitate visual discrimination between the near-overlapping coexisting curves for FtoA (red) and RtoK (green) in the Urry interaction scheme.

gram) for the same temperature and bulk salt concentration would be different for systems with a different bulk protein density. In this regard, the meaning of the phase diagrams in Fig. 7 is more restrictive than phase diagrams for one solute species in which the coexisting solute densities for a given temperature apply to all bulk solute densities within the two-phase region.

Results in Figs. 6 and 7 confirm and add to previous observations that LLPS properties entailed by different interaction schemes can be significantly different.^{66,111,117} Two-solute-species (ρ_p, ρ_s) phase properties of Ddx4 IDRs such as those depicted in Fig. 6 have not been considered before. A novel feature that emerges in Fig. 6 is that, for the KH and Mpipi interaction schemes, the coexistence curve for the CS variant (orange curve) intersects the coexistence curves of other Ddx4 variants (green and red curves), indicating that the rank ordering of LLPS propensities is predicted by these interaction schemes to be salt dependent. This is caused by the fact that the sequence electric charge pattern of CS is different from that of the other Ddx4 variants and therefore the electrostatic screening effects of salt on

CS phase separation vary in a different manner from that on the other Ddx4 variants when salt concentration varies. The same feature is manifested by the crossing between the CS coexistence curves and those of other variant(s) in the KH and Mpipi panels in Fig. 7, indicating that the rank ordering of LLPS propensities of the Ddx4 IDRs is predicted by these two interaction schemes to be temperature dependent as well.

As noted before,^{66,117} for KH and Mpipi, all three variants clearly exhibit lower LLPS propensities than the WT (the blue curve is farther to the right than the other curves in the KH and Mpipi panels in Fig. 6, and the blue curve for the condensed-phase protein density is higher than the other curves in the corresponding panels in Fig. 7). This trend is consistent with experiments.^{9,19,98} For the RtoK and FtoA variants, the trend is underpinned by the effective Flory χ parameter ratios $\chi_{\text{eff}}^{(\text{RtoK})}/\chi_{\text{eff}}^{(\text{WT})} = 0.83$, $\chi_{\text{eff}}^{(\text{FtoA})}/\chi_{\text{eff}}^{(\text{WT})} = 0.66$ for KH and $\chi_{\text{eff}}^{(\text{RtoK})}/\chi_{\text{eff}}^{(\text{WT})} = 0.80$, $\chi_{\text{eff}}^{(\text{FtoA})}/\chi_{\text{eff}}^{(\text{WT})} = 0.84$ for Mpipi in Eq. (60). In the Urry interaction scheme, the three Ddx4 variants also show lower LLPS propensities than that of the WT, but only barely for RtoK and FtoA ($\chi_{\text{eff}}^{(\text{RtoK})}/\chi_{\text{eff}}^{(\text{WT})} = 0.96$, $\chi_{\text{eff}}^{(\text{FtoA})}/\chi_{\text{eff}}^{(\text{WT})} = 0.97$ for Urry). In contrast, as pointed out before,⁶⁶ results for HPS in Figs. 6 and 7 indicate that the RtoK variant has a higher LLPS propensity than WT, which is inconsistent with experiments^{9,19,98} ($\chi_{\text{eff}}^{(\text{RtoK})}/\chi_{\text{eff}}^{(\text{WT})} = 1.09$, $\chi_{\text{eff}}^{(\text{FtoA})}/\chi_{\text{eff}}^{(\text{WT})} = 0.97$ for HPS). The results in Figs. 6 and 7 for FB also exhibit a higher LLPS propensity for RtoK than for WT, though to a lesser degree. Similar to HPS, this FB prediction ($\chi_{\text{eff}}^{(\text{RtoK})}/\chi_{\text{eff}}^{(\text{WT})} = 1.04$, $\chi_{\text{eff}}^{(\text{FtoA})}/\chi_{\text{eff}}^{(\text{WT})} = 0.94$ for FB) is caused by its exceptionally high hydrophobicity parameter of 0.47106 for lysine compared to that of 0.24025 for arginine (Table S7 for optimized FB-HPS parameters in ref. 112).

Experimental data on Ddx4 IDRs indicate that LLPS propensity of WT is higher than that of CS (ref. 9) and that LLPS propensity of CS is higher than that of FtoA (ref. 19, FtoA corresponds to 14FtoA in this reference). Because LLPS for FtoA is observed at $\sim 350 \text{ mg mL}^{-1}$ protein concentration but not for RtoK up to 400 mg mL^{-1} protein concentration under the conditions given in Appendix 1–Table 4 of ref. 98, the overall experimental rank ordering of LLPS propensities is $\text{WT} > \text{CS} > \text{FtoA} > \text{RtoK}$. Notably, this rank ordering is reproduced by Mpipi, as shown in Fig. 6b of ref. 117 and Figs. 6 and 7 here (red curves are higher than green curves for Mpipi), with $\chi_{\text{eff}}^{(\text{RtoK})}/\chi_{\text{eff}}^{(\text{FtoA})} = 0.95$ for Mpipi. By comparison, KH does not capture this trend entirely, as its predicted rank ordering of LLPS propensities is $\text{WT} > \text{CS} > \text{RtoK} > \text{FtoA}$ ($\chi_{\text{eff}}^{(\text{RtoK})}/\chi_{\text{eff}}^{(\text{FtoA})} = 1.26$ for KH), as shown in Fig. 4 of ref. 66 and in Figs. 6 and 7 here (red curves are lower than green curves for KH).

Field-Theoretic Simulations of Phase Behaviors of Model Hydrophobic-Polar Sequences with the Same Composition but Different Sequence Patterns. As a first test of the FTS approach introduced above for modeling sequence-dependent LLPS effects of spatially short-range interaction, we apply the formulation to three model hydrophobic-polar sequences with the same 3/2 hydrophobic/polar composition but different sequence

patterns of the hydrophobic and polar residues. We adopt three 20mer ($N = 20$) sequences with $f_T = 0.6$ from Statt et al.¹³² (hydrophobic composition is denoted as f_T in this reference), namely their “[HT]₂TH[T₂H]₄TH”, “T₃H₃T₃H₂T₃H₃T₃”, and “T₁₂H₈” sequences listed, respectively, as the last sequence in Fig. S6, the sequence in Fig. 5, and the “micelles” sequence in Fig. 6 in ref. 132. As mentioned above, since we use leucine and serine, respectively, for the hydrophobic and polar residues in the present study, we refer to these three sequences as LS1, LS2, and LS3 (Fig. 8a). For computational efficiency, we opted to use these short LS sequences without electrostatic interactions instead of the Ddx4 IDR sequences that are more than ten times longer for the first test of our FTS formulation. FTS of longer sequences with more complex interactions entails technical issues with regard to equilibration that remains to be tackled.

The hydrophobic and polar residues are more evenly distributed in LS1 and LS2 than in the diblock arrangement of LS3. Statt et al. essentially use a standard hydrophobic-polar (HP) potential¹⁵⁷ whereby only hydrophobic-hydrophobic interactions are favorable (governed by a LJ potential in the form of Eq. (46) with negative contact energy and excluded volume), polar-polar and polar-hydrophobic interactions are repulsive because of excluded volume (governed by a WCA potential¹⁴⁹). Within this HP interaction scheme, the LLPS critical temperatures ($T_{cr} = T_c$ in their notation) for the first and second sequences are, in model units, $T_{cr} = 0.808$ and $T_{cr} = 1.083$, whereas the third sequence apparently does not have a critical point (Table S1 of ref. 132). Since we will be applying the KH interaction scheme to the LS sequences, with $\mathcal{E}_{r_\alpha, r_\beta} = -0.771, 0$, and -0.304 , respectively, for $(r_\alpha, r_\beta) = (\text{leucine, leucine}), (\text{serine, serine}), (\text{leucine, serine})$, instead of the HP potential, LLPS behaviors of our LS sequences are expected to exhibit a similar but not identical trend to their corresponding HP-like sequences. The present choice of using the KH potential for leucine and serine—with nonzero interactions for all three possible interaction pairs instead of the HP interaction scheme which is diagonalized by construction with only one nonzero interaction—is motivated by our desire to test the new FTS formulation with a more complex interaction scheme that requires diagonalization of the $\varepsilon_{r, r'}$ matrix.

The FTS is performed on an $M = 48$ lattice with lattice spacing $\Delta x = a_s = b/\sqrt{6} \approx 1.6$ Å, which amounts to a simulation box with a linear dimension of ≈ 75 Å. Using the KH interaction matrix, we truncate the summations over eigenvalues at $\tilde{a} = 3$ [Eqs. (1) and (2)]. The range of spatially short-range interactions governed by $V_h(r)$ in Eq. (49) is set to $\kappa^{-1} = 5$ Å and we let $v_b = v_w = 1$ for simplicity. All simulations are performed without salt, and since the LS sequences carry no electric charge, the field $\psi(\mathbf{r})$ in Eq. (20) can be omitted. The total density of the system is set to $\rho_0 = \rho_w + N\rho_p = 55.5$ M, with a polymeric (LS sequence) component of $\rho_p = 300$ mM giving a polymer bead volume fraction of $\phi = 0.11$. The system thus contains $n_p \approx 75$ LS polymer chains and $n_w \approx 1.2 \times 10^4$ solvent molecules. We set the compressibility to $\gamma = 0.1b^{-3} \approx 3.0$ M because of equilibration issues observed in

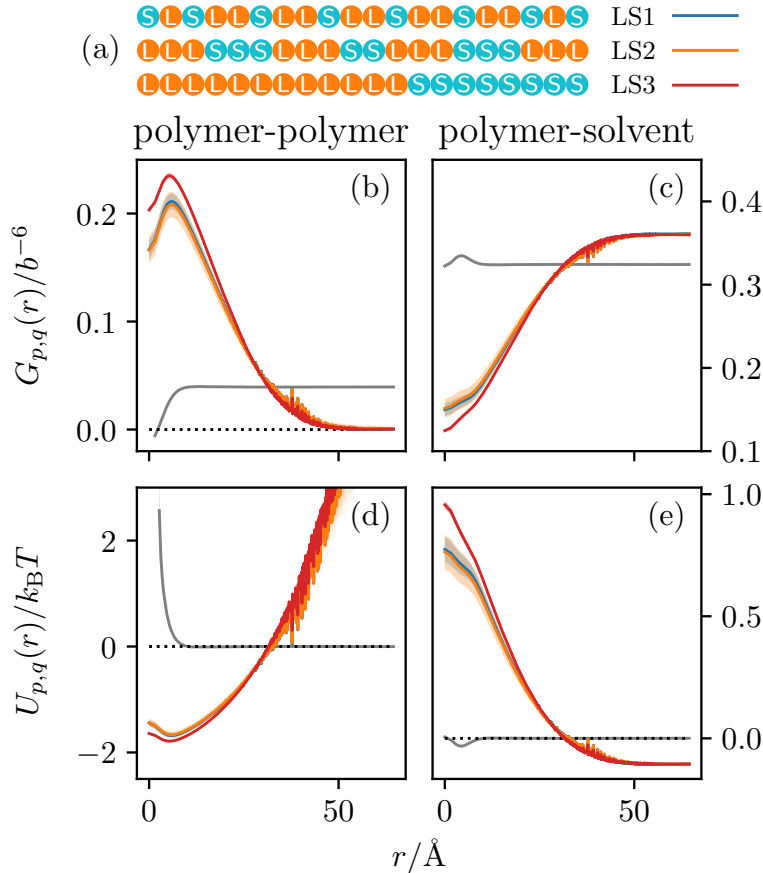


Fig. 8: Sequence-specific LLPS effects of hydrophobic-like short-spatial-range interactions. (a) Leucine-Serine (LS) 20mer polymer sequences used for FTS in this work. (b,c) Polymer-polymer and polymer-solvent pair correlation functions $G_{b,b}(r)$ and $G_{b,s}(r)$, defined in Eq. (50), computed in FTS ($p = b$, $q = s$). (d,e) PMFs computed from the pair-correlation functions in (a,b) using Eq. (51). Solid curves and shaded bands in panels (b–e) depict the average and standard deviation of twenty one independent simulations. The gray solid curve in each panel corresponds to $l_h = 0.03 \text{ \AA}$, wherein short-spatial-range interactions are not sufficiently strong to drive condensate formation and for which no visible sequence dependence is observed. Colored curves are computed at $l_h = 0.5 \text{ \AA}$ for which the strong short-spatial-range interactions cause the polymers to form a dense condensate.

FTS of exactly incompressible systems.⁹¹ However, we note that incompressible systems can alternatively be explored in FTS using the partial saddle-point approximation of ref. 164. Simulations are performed at $l_h = 0.5 \text{ \AA}$ ($\chi_{\text{eff}} = 2.16$) and at $l_h = 0.03 \text{ \AA}$ ($\chi_{\text{eff}} = 0.129$) corresponding, respectively, to strong and weak short-spatial-range interactions. The CL evolution equations in Eq. (38) are numerically solved with a time-step $\Delta t = 5 \times 10^{-4} b^3$ using a semi-implicit integration scheme¹⁶⁵ generalized to multiple fields.⁷⁸ We perform 21 independent simulations for each sequence and parameter set, and use $Q_{p,w}$ to monitor system equilibration. At $l_h = 0.5 \text{ \AA}$, the system requires 4×10^5 time-steps for equilibration,

after which the field configuration are sampled every 50th step during the production run consisting of another 4×10^5 CL steps. At $l_h = 0.03 \text{ \AA}$, 2×10^4 integration steps are sufficient for equilibration, followed by sampling every 50th step during a production run of 3×10^5 steps.

Fig. 8b–e shows pair-correlation functions and PMFs computed in FTS using Eqs. (50) and (51) for the three LS sequences. The grey curve in each panel corresponds to $l_h = 0.03 \text{ \AA}$, for which the system remains in a homogeneous (single-phase) state exhibiting no significant sequence dependence in the properties simulated. This single-phase state is characterized by all PMFs approaching zero at large r . Colored curves in Fig. 8 correspond to $l_h = 0.5 \text{ \AA}$, at which the short-spatial-range interactions are sufficiently strong to drive the system into an inhomogeneous state containing a single spherical polymer-dense condensate against a near polymer-empty background. This feature is characterized by the $G_{p,p}(r) \sim 0$ (Fig. 8b) at separations r larger than the condensate diameter, combined with polymer-solvent anti-correlation at small r because solvent are being pushed out of the condensate.

Sequence-dependent effects are exhibited by the correlation functions and the PMFs. While the sequences LS1 and LS2 behave very similarly (blue and orange curves essentially overlap in Fig. 8b–e), the diblock sequence LS3 stands out clearly by forming denser condensates than both LS1 and LS2 (at small r , the red curve is higher than the orange and blue curves for correlation functions in Fig. 8b; and the red curve is lower than the orange and blue curves for PMFs in Fig. 8d). We also find that the LS3 condensate possesses a more heterogeneous internal structure with distinct sub-regions populated predominantly by either L or S residues. This feature can be seen in the simulation snapshots in Figs. 9 and 10, which depict the real component of the field operators

$$\tilde{\rho}_X(\mathbf{r}) = \frac{\rho_p}{Q_p} \sum_{\alpha=1}^N e^{W_\alpha(\mathbf{r})} q_F(\mathbf{r}, \alpha) q_B(\mathbf{r}, \alpha) \delta_{r,\alpha,X}, \quad X = \text{L (leucine), S (serine)}, \quad (61)$$

for the number density of L and S residues (the Kronecker $\delta_{r,r'} = 1$ for $r = r'$ and $\delta_{r,r'} = 0$ for $r \neq r'$). To facilitate visualization of the condensate structure, the snapshots in Fig. 9 are averaged over 10^3 consecutive CL time steps. Fig. 10 provides cross-sectional views through the center of mass of each of the snapshots in Fig. 9. Leucine and serine densities are represented by contours in Fig. 10 following the style introduced by Fig. 3 of ref. 62. The contour plots in Fig. 10 demonstrate a marked increased degree of structural heterogeneity of the LS3 condensate relative to the LS1 and LS2 condensates. For LS3, the serine (polar) residues are predominantly on the outside whereas the leucine (hydrophobic) residues are predominantly inside. This phenomenon is reminiscent of micellar structure and, in this regard, consistent with the simulated structure of the corresponding hydrophobic-polar sequence in ref. 132. A similar behavior has been observed in Monte-Carlo simulations of 10mer hydrophobic-polar sequences, where the sequence of alternating hydrophobic-polar

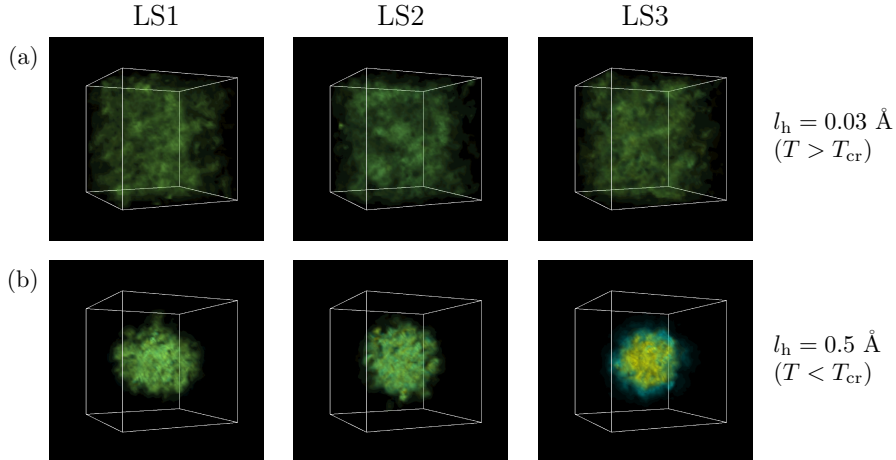


Fig. 9: Field snapshots illustrate LLPS of LS sequences. Snapshots of FTS after equilibration, showing field operators corresponding to leucine and serine number densities in orange and cyan, respectively. The left, middle and right columns are for the sequences LS1, LS2 and LS3, respectively, in Fig. 8a. (a) Top panels show snapshots under conditions where interactions are not sufficiently strong to cause condensation ($T > T_{\text{cr}}$, where T_{cr} is upper critical solution temperature, UCST). (b) Bottom panels depict systems under conditions where there are sufficiently strong interactions for phase separation ($T < T_{\text{cr}}$). All snapshots are averaged over 10^3 CL steps.

residues underwent LLPS whereas the diblock condensate exhibited micellar structure instead.⁶¹

Assessing Analytical and FTS Results by Coarse-Grained Explicit-Chain MD. We now proceed to further evaluate the effectiveness of the above analytical and FTS approaches by comparing their predictions with the corresponding results from coarse-grained explicit-chain models. As described in Models and Methods, while field-theoretic formulation and coarse-grained modeling aim to capture essential physics of the same system, details of the two types of models differ. For instance, on one hand, the functional form of residue-residue interactions is practically limited in field-theoretic formulation because of mathematical consideration—in the present case we are restricted to a single Yukawa form for all residue pairs, i.e., using $V_h(r)$ in Eq. (49) with the same l_h and κ for all amino acid pairs. In contrast, there is more freedom in selecting functional forms for potential energy (e.g., Lennard-Jones, Ashbaugh-Hatch, Wang-Frenkel) as well as using different bead sizes to represent different amino acid residues; e.g., different $\sigma_{\alpha,\beta}$ for different types of amino acid pairs r_α, r_β in Eq. (56). On the other hand, it is computationally much more efficient to account for explicit solvent in field-theoretic approaches than in MD. This recognition notwithstanding, to be useful as a computationally efficient approach

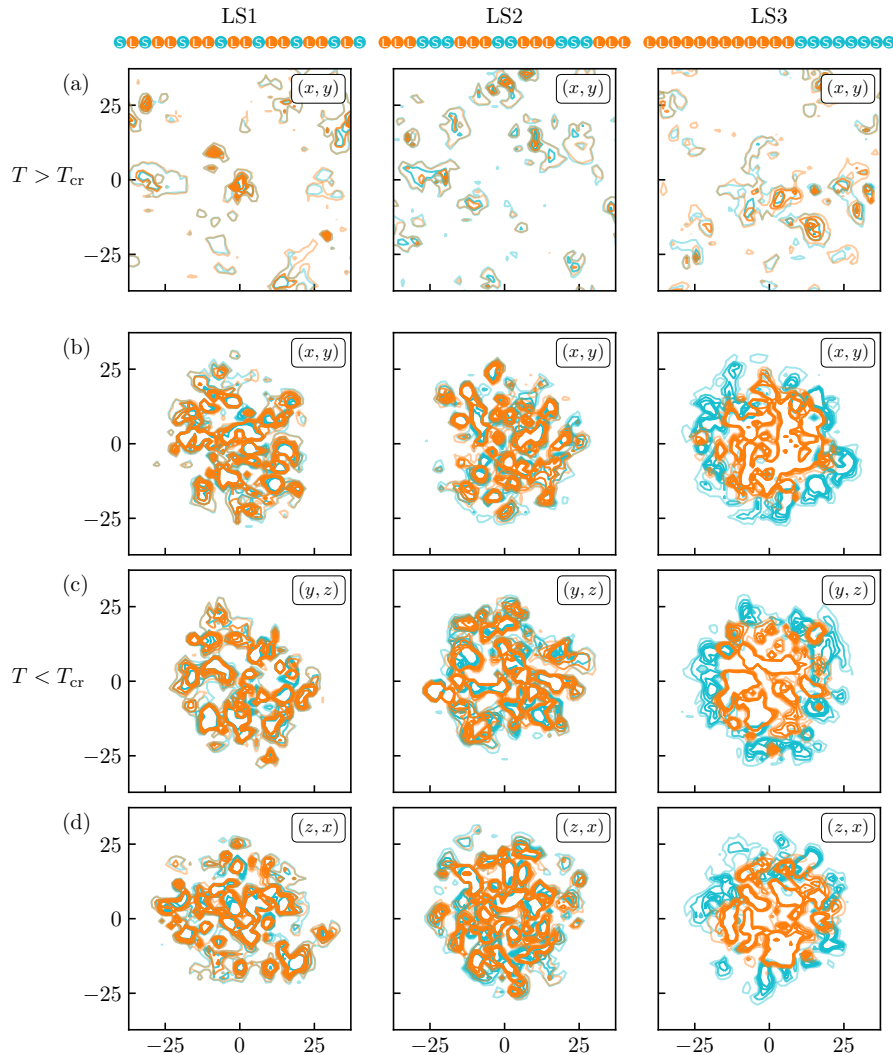


Fig. 10: Internal structure of condensates of model hydrophobic-polar sequences. Cross-sectional density distributions of the snapshots in Fig. 9 in planes indicated by the insets, with x , y , and z coordinates plotted in units of \AA . Leucine and serine densities are shown in orange and cyan, respectively, as in Fig. 9. (a) Snapshots at $l_h = 0.03 \text{ \AA}$ where the systems remain in a single-phase state. (b–d) Snapshots at $l_h = 0.5 \text{ \AA}$ where the LS polymers coalesce into a near-spherical condensate.

complementary to coarse-grained explicit-chain MD, field-theoretic method applied to any given system should produce results that are in agreement, at least semi-quantitatively, with those obtained from an appropriately constructed coarse-grained explicit-chain model for the same system. In future investigations, it will be interesting to explore possible tuning of energetic parameters in our analytical and FTS formulations to optimize agreement with coarse-grained explicit-chain MD and/or experimental data to enable more broadly practical applications of field-theoretic techniques.

Coarse-Grained Explicit-Chain MD for Ddx4 IDRs. With this in mind, phase diagrams for the four Ddx4 IDRs are obtained by coarse-grained explicit-chain MD using the Mpipi,¹¹⁷ Urry,¹¹¹ and FB¹¹² interaction schemes (Fig. 11). Corresponding coarse-grained explicit-chain MD phase diagrams using KH and HPS have been provided, respectively, in Fig. 4 and Fig. 3B of ref. 66. The trends exhibited by these coarse-grained MD results are largely consistent with the analytical MFT/RPA results in Figs. 6 and 7, suggesting that the MFT/RPA formulation is a computationally efficient approach for exploring sequence-dependent LLPS of IDPs. In particular, in agreement with Fig. 6b of the original Mpipi study¹¹⁷ (dotted curves in Fig. 11a, which were computed by using $\kappa_D^{-1} = 7.95 \text{ \AA}$, $\epsilon_r = 80$ instead of the $\kappa_D^{-1} = 10 \text{ \AA}$, $\epsilon_r = 40$ values used for the solid curves in Fig. 11a here) and consistent with the present analytical MFT/RPA results in Fig. 7 at lower model temperatures $T \lesssim 250 \text{ K}$, Fig. 11a exhibits the experimentally correct WT > CS > FtoA > RtoK rank ordering of LLPS propensities,^{9,19,98} though the Mpipi-computed difference in LLPS propensity between WT and CS ($\sim 6\text{--}10 \text{ K}$ difference in T_{cr})¹¹⁷ is significantly smaller than the experimental estimation of $\sim 80 \text{ K}$ difference in T_{cr} at $[\text{NaCl}] = 100 \text{ mM}$ (ref. 19). For Urry, the LLPS propensity rank ordering WT > FtoA \approx RtoK > CS computed by coarse-grained MD (Fig. 11b) is consistent with that for Urry in MFT/RPA Figs. 6 and 7. Similarly, for FB, the RtoK > WT > FtoA > CS rank ordering in Fig. 11c is consistent with that for FB in Figs. 6 and 7. A comparison of the global critical temperatures computed by analytical MFT/RPA and those simulated using coarse-grained MD at a fixed monovalent salt concentration of $\sim 100 \text{ mM}$ for the interaction schemes Mpipi, Urry, and FB is provided in Fig. 12.

As discussed in previous works,^{66,111,112,117} some of the salient differences among interaction schemes can be understood semi-quantitatively by simple considerations of the schemes' contact energies. For instance, the differences in LLPS behavior of the RtoK variant across different interaction schemes are clearly related to the average strength of interactions involving R versus that involving K in the interaction schemes. For Mpipi, consider the average $\mathcal{E}_{\text{R,K}} \equiv \sum_{r=1}^{20} \mathcal{E}_{r,r'}/20$ over the 20 amino acid types, where r' is the label for arginine (R) or lysine (K). Entries for $\mathcal{E}_{r,r'}$ in Supplementary Table 11 of ref. 117 yield $\mathcal{E}_{\text{R}} = 0.2212 \text{ kcal mol}^{-1}$ and $\mathcal{E}_{\text{K}} = 0.0563 \text{ kcal mol}^{-1}$, thus $\Delta\mathcal{E}_{\text{R-K}} \equiv \mathcal{E}_{\text{R}} - \mathcal{E}_{\text{K}} = 0.1649 \text{ kcal mol}^{-1}$ may be used to characterize the degree to which interactions involving R are more favorable than those involving K. The corresponding quantity in KH is $\Delta(\lambda^{\text{hh}}\mathcal{E})_{\text{R-K}} = 0.0829 \text{ kcal mol}^{-1}$, which is significantly smaller. Here, for KH, $\Delta(\lambda^{\text{hh}}\mathcal{E})_{\text{R-K}} \equiv (\lambda^{\text{hh}}\mathcal{E})_{\text{R}} - (\lambda^{\text{hh}}\mathcal{E})_{\text{K}}$, with $\lambda^{\text{hh}}\mathcal{E}_{\text{R,K}} \equiv -\sum_{r=1}^{20} \lambda_{r,r'}^{\text{hh}}\mathcal{E}_{r,r'}/20$, and $-\lambda_{r,r'}^{\text{hh}}\mathcal{E}_{r,r'}$ being the entries in Table S3 of ref. 40. For HPS, Urry, and FB, the corresponding difference in interaction strength is given by $\mathcal{E}\Delta\lambda_{\text{R-K}}/2 \equiv \mathcal{E}[\lambda(\text{R}) - \lambda(\text{K})]/2$ where $\mathcal{E} = 0.2 \text{ kcal mol}^{-1}$ and $\lambda(\text{R})$ and $\lambda(\text{K})$ are, respectively, the value for R and K on a given hydrophobicity/hydrophathy scale (see Models and Methods). From the scales in Table S1 of ref. 40, the ‘‘Urry et al.’’ column of Table S2 of

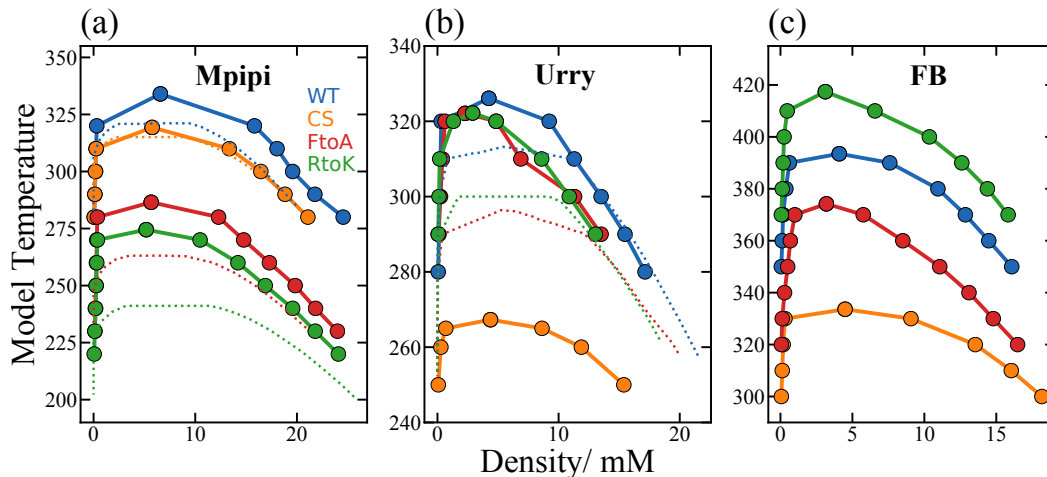


Fig. 11: Comparing explicit-chain model phase behaviors of Ddx4 IDRs in different interaction schemes. Phase diagrams (coexistence curves) for WT (blue), CS (orange), FtoA (red), and RtoK (green) are obtained by coarse-grained MD at $\epsilon_r = 40$ using the (a) Mpipi,¹¹⁷ (b) Urry,¹¹¹ or (c) FB¹¹² interaction schemes in accordance with the modeling details and simulation procedure described in Models and Methods. Solid lines passing through simulation data points and extrapolated critical points^{40,66,67} (filled circles) are a guide for the eye. Dotted lines (same color code) are previously simulated coexistence curves adapted from Fig. 6b of ref. 117 (a) and Fig. 4a of ref. 111 (b) to facilitate comparison.

ref. 111, and Table S7 of ref. 112, $\mathcal{E}\Delta\lambda_{R-K}/2 = -0.0514, 0.0176,$ and -0.0231 kcal mol⁻¹, respectively, for HPS, Urry, and FB. Taken together, these numbers for Mpipi, KH, Urry, HPS, and FB, viz., 0.1807, 0.0829, 0.0176, $-0.0459,$ and -0.0170 respectively, provide a useful explanation for the signs and magnitudes of their WT – RtoK critical temperature differences $\Delta(T_{cr})_{WT-RtoK} \equiv (T_{cr})_{WT} - (T_{cr})_{RtoK} \approx 60, 43, 4, -29,$ and -24 K as seen for Mpipi, KH, Urry, HPS, and FB, respectively, in Fig. 11 of the present study as well as in Fig. 3B and Fig. 4 of ref. 66.

As noted above, the difference in LLPS propensity between WT and CS predicted by Mpipi is small, with $\Delta(T_{cr})_{WT-CS} \approx 6$ K in the original simulation¹¹⁷ and ≈ 15 K in Fig. 11a, both much less than the experimentally estimated $\Delta(T_{cr})_{WT-CS} \sim 80$ K (refs. 19). In fact, the slightly higher $\Delta(T_{cr})_{WT-CS}$ we obtain is probably due in large part to the smaller dielectric constant $\epsilon_r = 40$ used for Fig. 11a instead of the $\epsilon_r = 80$ value used in the original study. By comparison, larger $\Delta(T_{cr})_{WT-CS}$ values are predicted by most of the other interaction schemes considered here: For HPS, $\Delta(T_{cr})_{WT-CS} \approx 14$ K for $\epsilon_r = 80$ (Fig. 3B of ref. 66). For KH, $\Delta(T_{cr})_{WT-CS} \approx 21$ and 46 K, respectively, for $\epsilon_r = 80$ and 40 (Fig. 4 of ref. 66). For Urry and FB simulated here at $\epsilon_r = 40$, $\Delta(T_{cr})_{WT-CS} \approx 60$ K (Fig. 11b,c). Presumably, this conspicuous difference between Mpipi and the other interaction schemes regarding CS properties is chiefly caused by Mpipi’s electric charge assignment of $0.75e$ for R and K, $-0.75e$ for aspartic acid (D) and glutamic acid (E), and $0.375e$ for histidine¹¹⁷ instead of using the full proton charge e for electrostatic interactions among R, K, D, and E as in

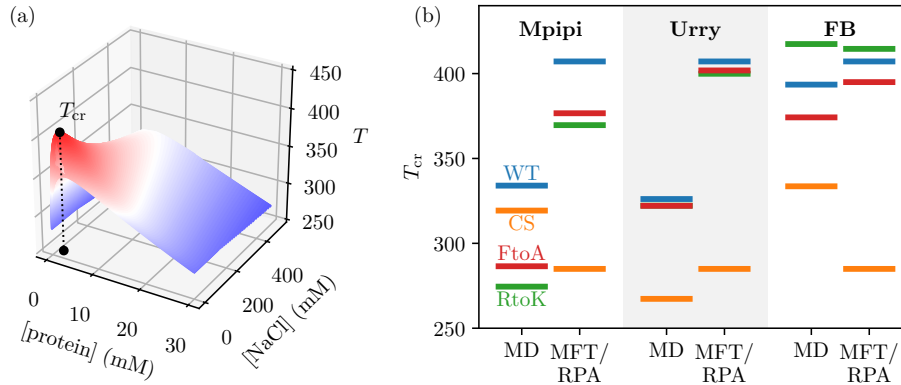


Fig. 12: Comparing the critical temperature T_{cr} in the coarse-grained explicit-chain MD and the analytical MFT/RPA models. (a) An example of [protein]-[salt]-temperature phase diagrams computed in the approximate analytical MFT/RPA theory for WT Ddx4 IDR using Mpipi. The depicted binodal surface is constructed by stacking [protein]-[salt] coexistence curves at constant T (i.e. solid curves in Fig. 6) at heights corresponding to their respective temperatures. The indicated global critical temperature, T_{cr} , is found by maximizing the function $T(\rho_p, \rho_s)$ defined implicitly through $\det \mathcal{H} = 0$ where \mathcal{H} is a 2×2 Hessian matrix with entries $\partial^2 f / \partial \rho_i \partial \rho_j$, and $i, j = p, s$, (ref. 78). The vertical dotted line shows the projection of the critical point onto the [protein]-[salt] plane, indicating the corresponding critical densities. (b) The rank orderings of T_{cr} for the Ddx4 IDRs in coarse-grained MD in Fig. 11 and the global T_{cr} in MFT/RPA mostly agree for each of the three interaction schemes. Note that the discrepancies in the magnitudes of MD- and MFT/RPA-predicted T_{cr} values shown here are largely a consequence of different energy scales used for MD and MFT/RPA. As stated in the discussion above for the results in Fig. 6, in order to facilitate comparison across different interaction schemes, the chosen energy scales for MFT/RPA are such that χ_{eff} is always equal to 0.5 at a reference temperature $T = 300\text{K}$ and $l_B = 7 \text{ \AA}$ for WT Ddx4 for all interaction schemes (thus all the blue lines for MFT/RPA in (b) are at the same level). In contrast, we largely follow the full interaction potentials provided in refs. 111, 112 and 117 for the Urry, FB, and Mpipi interaction schemes. It follows that only the rank orderings—but not the magnitudes—of T_{cr} s for the Ddx4 variants are comparable in (b).

the other interaction schemes. Since each of the Ddx4 IDRs contains only two histidines, the main effects are in R, K, D, and E. The assignment of $\pm 0.75e$ electric charges instead of $\pm e$ amounts to a reduction factor $(0.75)^2 = 0.5625$ in electrostatic interaction strength, which is further attenuated by Mpipi’s adoption of a slightly shorter Debye screening length $\kappa_D^{-1} = 7.95 \text{ \AA}$ instead of the $\kappa_D^{-1} = 10 \text{ \AA}$ employed for the other interaction schemes. Because the difference in LLPS propensity between WT and CS is principally a sequence-specific electrostatic effect, Mpipi’s reduced electrostatic strength should go a long way in accounting for the relatively small $\Delta(T_{cr})_{WT-CS}$ it predicts.

Secondary to electrostatics, another possible origin of the observed variation in $\Delta(T_{cr})_{WT-CS}$ predicted by different interaction schemes is their different spatially short-range nonelectrostatic residue-residue contact energies. WT is transformed into CS, and vice versa, by swapping residues among 24 sequence positions—involving 6 D, 6 E, 9 R, and 3 K residues participating in 4 (E \leftrightarrow R), 5 (D \leftrightarrow R), 2 (E \leftrightarrow K), and 1 (D \leftrightarrow K)

interchanges. Because the D, E, R, and K residues engage in nonelectrostatic as well as electrostatic interactions, sequence-specific nonelectrostatic interactions do contribute to $\Delta(T_{cr})_{WT-CS}$ and this effect clearly depends on the interaction scheme. Now, the energetic effects of the (E \leftrightarrow R), (D \leftrightarrow R), (E \leftrightarrow K), and (D \leftrightarrow K) swaps may be characterized by $\mathcal{E}\Delta\lambda_{E-R}/2$, $\mathcal{E}\Delta\lambda_{D-R}/2$, $\mathcal{E}\Delta\lambda_{E-K}/2$, and $\mathcal{E}\Delta\lambda_{D-K}/2$; but these quantities can have different magnitudes and even different signs for different interaction schemes, as exemplified by the $\mathcal{E}\Delta\lambda_{E-R}/2$, $\mathcal{E}\Delta\lambda_{D-R}/2$, $\mathcal{E}\Delta\lambda_{E-K}/2$, and $\mathcal{E}\Delta\lambda_{D-K}/2$ values of 0.0459, 0.0378, -0.0055 , and -0.0136 kcal mol $^{-1}$, respectively, for HPS, the corresponding values of -0.0558824 , -0.0264705 , -0.0382354 , and -0.0088235 kcal mol $^{-1}$ for Urry, and 0.018596, 0.0065, -0.004485 , and -0.016581 for FB. Ramifications of these differences on the LLPS properties of model CS Ddx4 IDR remain to be further explored.

Coarse-Grained Explicit-Chain MD for Hydrophobic-Polar Sequences. Fig. 13 provides phase behaviors computed by explicit-chain MD simulation for the three LS sequences studied above by FTS. The rank ordering of LLPS propensity $LS3 > LS2 \gtrsim LS1$ observed in Fig. 13a is consistent with that deduced from FTS correlation functions and PMFs in Fig. 8, attesting to the effectiveness of the FTS formulation developed here for sequence-specific effects of spatially short-range interactions on LLPS of IDPs. There are minor differences between the FTS and MD results, in that the FTS correlation functions and PMFs suggest that the LLPS propensities of LS1 and LS2 are practically identical considering numerical uncertainties, but the MD phase diagrams show that LS2 has a slightly higher LLPS propensity than LS1. Such minor differences are not unexpected given the differences discussed above between the FTS and MD models. In both our FTS and MD models, the more blocky LS3 sequence clearly exhibits its superior LLPS propensity.

The critical temperatures of the LS sequences shown in Fig. 13a are 3–4 times higher than those of the Ddx4 IDRs in Fig. 11, exhibiting stable droplets at model temperatures as high as 1000 K (Fig. 13b–d). This observation is notable because LLPS propensities tend to increase with chain length³⁶ but the LS sequences have a much shorter chain length ($N = 20$) than that of the Ddx4 IDRs ($N = 236$). A likely reason for the high LLPS propensities of the LS sequences is the strongly favorable leucine-leucine interaction (strongest in the KH scheme) and favorable leucine-serine interactions in the model. The snapshot in Fig. 13d for LS3 shows a certain degree of separate clustering of the leucine residues and of the serine residues, but not to the extent displayed by the micellar organization of the corresponding hydrophobic-polar sequence in ref. 132, probably because the leucine-serine interaction is favorable in our KH interaction scheme (and thus conducive to leucine-serine mixing) but the interaction between a hydrophobic and a polar bead is repulsive in ref. 132.

A sequence hydrophathy decoration (SHD) parameter, defined as $SHD = N^{-1} \sum_{\alpha < \beta}^N [\lambda(r_{\alpha}) + \lambda(r_{\beta})] |\alpha - \beta|^{-1}$, was proposed recently as a predictor of prop-

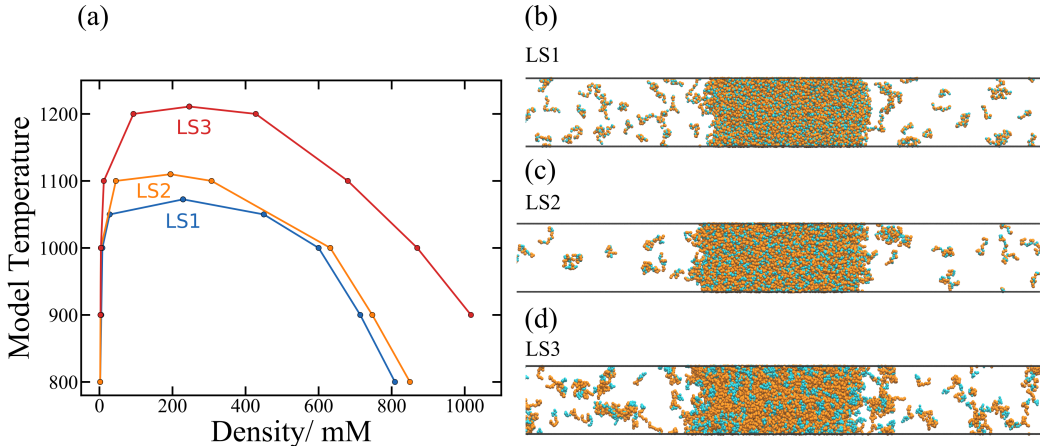


Fig. 13: Sequence-dependent phase behaviors of hydrophobic-polar sequences in our explicit-chain model. (a) Phase diagrams (coexistence curves) of the three leucine-serine sequences LS1, LS2, and LS3 in Fig. 8a are computed by coarse-grained MD using the KH interaction scheme⁴⁰ and the protocol described in Models and Methods. Simulation data points and extrapolated critical points^{40,66,67} are shown as filled circles, connecting lines are a guide for the eye. (b–d) Snapshots taken during the simulation showing a part of the simulation box for 1,000 copies of (b) LS1 at model temperature $T = 1000$ K, (c) LS2 at model $T = 1000$ K, and (d) LS3 at model $T = 1200$ K. Beads representing leucine and serine are shown, respectively, in orange and cyan in these snapshots. Significant number of polymers are seen in the dilute phase of each of these systems.

erties of single-chain conformational ensembles of heteropolymers.¹⁰² For applications to interaction schemes such as KH and Mpipi that have 210 contact energies instead of a 20-value hydrophobicity/hydropathy scale, we consider a natural generalization of the above formula:

$$\text{SHD} \rightarrow \text{SHD}^{\text{hh}} \equiv -N^{-1} \sum_{\alpha < \beta}^N \varepsilon_{r_\alpha, r_\beta} |\alpha - \beta|^{-1}, \quad (62)$$

where $\varepsilon_{r, r'}$ for KH is given by the entries in Table S3 of ref. 40. For the LS1, LS2, and LS3 sequences we consider here in the KH interaction scheme, $\text{SHD}^{\text{hh}} = 1.12$, 1.05, and 1.17, respectively. As the SHD^{hh} value of LS3 with higher LLPS propensity is larger than those of LS1 and LS2, this result suggests that SHD or SHD^{hh} may be used as a predictor for LLPS as well. Further effort will be needed to examine whether the correlation between SHD or SHD^{hh} and LLPS propensity of heteropolymers with spatially short-range interactions is as strong as that between sequence charge decoration (SCD)⁸⁶ and LLPS propensity of polyampholytes.^{39,41,43}

CONCLUSIONS

In summary, we have developed a field-theoretic formulation for modeling sequence-

specific biomolecular phase separation. Our theory offers a coarse-grained account of short-spatial-range π -related and hydrophobic interactions as well as long-spatial-range Coulomb interactions. In conjunction with RPA for electrostatics, a mean-field approximation for spatially short-range interactions derived from the general theory is useful as a computationally efficient tool for studying phase separation of intrinsically disordered proteins, as exemplified by the application to the Ddx4 IDRs described here. Full sequence effects of spatially short-range interactions can be studied using FTS, illustrated here by the sequence-dependent phase properties of three different hydrophobic-polar sequences with the same hydrophobic/polar composition. Initial success in applying these approaches to several different interaction schemes for modeling biomolecular LLPS are confirmed by coarse-grained explicit-chain molecular dynamics simulations. We have included only Yukawa potentials in our theory for this initial effort. Because ostensibly small changes in coarse-grained interaction potentials can lead to fundamental variations in conformational properties,^{166–168} future effort should aim to extend our formulation to other functional forms for spatially short-range potentials,¹⁵¹ including temperature-dependent effects.^{139,167} Techniques should also be further developed to study longer sequences of biological IDRs by FTS. Much exciting work lies ahead under the present theoretical framework.

Acknowledgements. We thank Yi-Hsuan Lin for helpful discussions. Financial support for this work was provided by Canadian Institutes of Health Research grant NJT-155930 and Natural Sciences and Engineering Research Council of Canada Discovery grant RGPIN-2018-04351 to H.S.C. We are grateful for the computational resources provided generously to our research group by Compute/Calcul Canada and the Digital Research Alliance of Canada.

The authors declare no conflict of interest.

References

- ¹ Banani, S. F.; Lee, H. O.; Hyman, A. A.; Rosen, M. K. Biomolecular condensates: organizers of cellular biochemistry. *Nat. Rev. Mol. Cell Biol.* **2017**, *18*, 285–298.
- ² Shin, Y.; Brangwynne, C.P. Liquid phase condensation in cell physiology and disease. *Science* **2017**, *357*, eaaf4382.

- ³ Lyon, A. S.; Peeples, W. B.; Rosen, M. K. A framework for understanding the functions of biomolecular condensates across scales. *Nat. Rev. Mol. Cell Biol.* **2021**, *22*, 215–235.
- ⁴ Jain, S.; Wheeler, J. R.; Walters, R. W.; Agrawal, A.; Barsic, A.; Parker, R. ATPase-modulated stress granules contain a diverse proteome and substructure. *Cell* **2016**, *164*, 487–498.
- ⁵ Wilson, E. B. The structure of protoplasm. *Science* **1899**, *10*, 33–45.
- ⁶ Brangwynne, C. P.; Eckmann, C. R.; Courson, D. S.; Rybarska, A.; Hoegel, C.; Gharakhani, J.; Jülicher, F.; Hyman, A. A. Germline P granules are liquid droplets that localize by controlled dissolution/condensation. *Science* **2009**, *324*, 1729–1732.
- ⁷ Li, P.; Banjade, S.; Cheng, H. C.; Kim, S.; Chen, B.; Guo, L.; Llaguno, M.; Hollingsworth, J. V.; King, D. S.; Banani, S. F.; Russo, P. S.; Jiang, Q.-X.; Nixon, B. T.; Rosen, M. K. Phase transitions in the assembly of multivalent signalling proteins. *Nature* **2012**, *483*, 336–340.
- ⁸ Kato, M.; Han, T. W.; Xie, S.; Shi, K.; Du, X.; Wu, L. C.; Mirzaei, H.; Goldsmith, E. J.; Longgood, J.; Pei, J.; Grishin, N. V.; Franz, D. E.; Schneider, J. W.; Chen, S.; Li, L.; Sawaya, M. R.; Eisenberg, D.; Tycko, R.; McKnight, S. L. Cell-free formation of RNA granules: low complexity sequence domains form dynamic fibers within hydrogels. *Cell* **2012**, *149*, 753–767.
- ⁹ Nott, T. J.; Petsalaki, E.; Farber, P.; Jarvis, D.; Fussner, E.; Plochowietz, A.; Craggs, T. D.; Bazett-Jones, D. P.; Pawson, T.; Forman-Kay, J. D.; Baldwin, A. J. Phase transition of a disordered nuage protein generates environmentally responsive membraneless organelles. *Mol. Cell* **2015**, *57*, 936–947.
- ¹⁰ Molliex, A.; Temirov, J.; Lee, J.; Coughlin, M.; Kanagaraj, A. P.; Kim, H. J.; Mittag, T.; Taylor, J. P. Phase separation by low complexity domains promotes stress granule assembly and drives pathological fibrillization. *Cell* **2015**, *163*, 123–133.
- ¹¹ Elbaum-Garfinkle, S.; Kim, Y.; Szczepaniak, K.; Chen, C. C.-H.; Eckmann, C. R.; Myong, S.; Brangwynne, C. P. The disordered P granule protein LAF-1 drives phase separation into droplets with tunable viscosity and dynamics. *Proc. Natl. Acad. Sci. U.S.A.* **2015**, *112*, 7189–7194.
- ¹² Lin, Y.; Protter, D. S. W.; Rosen, M. K.; Parker, R. Formation and maturation of phase-separated liquid droplets by RNA-binding proteins. *Mol. Cell* **2015**, *60*, 208–219.
- ¹³ Bergeron-Sandoval, L.P.; Safaei, N.; Michnick, S. W. Mechanisms and consequences of macromolecular phase separation. *Cell* **2016**, *165*, 1067–1079.
- ¹⁴ Li, X.-H.; Chavali, P. L.; Pancsa, R.; Chavali, S.; Babu, M. M. Function and regulation of phase-separated biological condensates. *Biochemistry* **2018**, *57*, 2452–2461.
- ¹⁵ Boeynaems, S.; Alberti, S.; Fawzi, N. L.; Mittag, T.; Polymenidou, M.; Rousseau, F.; Schymkowitz, J.; Shorter, J.; Wolozin, B.; Van Den Bosch, L.; Tompa, P.; Fuxreiter, M. Protein phase separation: a new phase in cell biology. *Trends Cell Biol.* **2018**, *28*, 420–435.
- ¹⁶ Cinar, H.; Fetahaj, Z.; Cinar, S.; Vernon, R. M.; Chan, H. S.; Winter, R. Temperature, hydrostatic pressure, and osmolyte effects on liquid-liquid phase separation in protein condensates:

- Physical chemistry and biological implications. *Chem. Eur. J.* **2019**, *57*, 13049–13069.
- ¹⁷ Gomes, E., and Shorter, J. The molecular language of membraneless organelles. *J. Biol. Chem.* **2019**, *294*, 7115–7127.
- ¹⁸ Burke, K. A.; Janke, A. M.; Fhine, C. L.; Fawzi, N. L. Residue-by-residue view of *in vitro* FUS granules that bind the C-terminal domain of RNA polymerase II. *Mol. Cell* **2015**, *60*, 231–241.
- ¹⁹ Brady, J. P.; Farber, P. J.; Sekhar, A.; Lin, Y.-H.; Huang, R.; Bah, A.; Nott, T. J.; Chan, H. S.; Baldwin, A. J.; Forman-Kay, J. D.; Kay, L. E. Structural and hydrodynamic properties of an intrinsically disordered region of a germ cell-specific protein on phase separation. *Proc. Natl. Acad. Sci. U.S.A.* **2017**, *114*, E8194–E8203.
- ²⁰ Kato, M.; McKnight, S. L. A solid-state conceptualization of information transfer from gene to message to protein. *Annu. Rev. Biochem.*, **2018**, *87*, 351–390.
- ²¹ Feric, M.; Vaidya, N.; Harmon, T. S.; Mitrea, D. M.; Zhu, L.; Richardson, T. M.; Kriwacki, R. W.; Pappu, R. V.; Brangwynne, C. P. Coexisting liquid phases underlie nucleolar subcompartments. *Cell* **2016**, *165*, 1686–1697.
- ²² Lin, Y. -H.; Brady, J. P.; Forman-Kay J. D.; Chan, H. S. Charge pattern matching as a ‘fuzzy’ mode of molecular recognition for the functional phase separations of intrinsically disordered proteins. *New J. Phys.* **2017**, *19*, 115003.
- ²³ Jülicher, F.; Grill, S. W.; Salbreux, G. Hydrodynamic theory of active matter. *Rep. Prog. Phys.* **2018**, *81*, 076601.
- ²⁴ Bertrand, T.; Lee, C. F. Diversity of phase transitions and phase separations in active fluids. *Phys. Rev. Res.* **2022**, *4*, L022046.
- ²⁵ Rosowski, K. A.; Sai, T.; Vidal-Henriquez, E.; Zwicker, D.; Style, R. W.; Dufresne, E. R. Elastic ripening and inhibition of liquid–liquid phase separation. *Nat. Phys.* **2020**, *16*, 422–425.
- ²⁶ Zhou, H.-X. Viscoelasticity of biomolecular condensates conforms to the Jeffreys model. *J. Chem. Phys.* **2021**, *154*, 041103.
- ²⁷ Sanchez-Burgos, I.; Joseph, J. A.; Collepardo-Guevara, R.; Espinosa, J. R. Size conservation emerges spontaneously in biomolecular condensates formed by scaffolds and surfactant clients. *Sci. Rep.* **2021**, *11*, 15241.
- ²⁸ Harmon, T. S.; Holehouse, A. S.; Rosen, M. K.; Pappu, R. V. Intrinsically disordered linkers determine the interplay between phase separation and gelation in multivalent proteins. *eLife* **2017**, *6*, e30294.
- ²⁹ Lin, Y.-H.; Forman-Kay, J. D.; Chan, H. S. Theories for sequence-dependent phase behaviors of biomolecular condensates. *Biochemistry* **2018**, *57*, 2499–2508.
- ³⁰ McSwiggen, D. T.; Mir, M.; Darzacq, X.; Tjian, R. Evaluating phase separation in live cells: Diagnosis, caveats, and functional consequences. *Genes Dev.* **2019**, *33*, 1619–1634.
- ³¹ Musacchio, A. On the role of phase separation in the biogenesis of membraneless compartments. *EMBO J.* **2022**, *41*, e109952.

- ³² Mittag, T.; Pappu, R. V. A conceptual framework for understanding phase separation and addressing open questions and challenges. *Mol. Cell* **2022**, *82*, 2201–2214.
- ³³ Lin, Y.-H.; Wu, H.; Jia, B.; Zhang, M.; Chan, H. S. Assembly of model postsynaptic densities involves interactions auxiliary to stoichiometric binding. *Biophys. J.* **2022**, *121*, 157–171.
- ³⁴ Hyman, A. A.; Weber, C. A.; Jülicher, F. Liquid-liquid phase separation in biology. *Annu. Rev. Cell Dev. Biol.* **2014**, *30*, 39–58.
- ³⁵ Brangwynne, C. P.; Tompa, P.; Pappu, R. V. Polymer physics of intracellular phase transitions. *Nat. Phys.* **2015**, *11*, 899–904.
- ³⁶ Lin, Y.-H.; Forman-Kay, J. D.; Chan, H. S. Sequence-specific polyampholyte phase separation in membraneless organelles. *Phys. Rev. Lett.*, **2016**, *117*, 178101.
- ³⁷ Vovk, A.; Gu, C.; Opferman, M. G.; Kapinos, L. E.; Lim, R. Y. H.; Coalson, R. D.; Jasnow, D.; Zilman, A. Simple biophysics underpins collective conformations of the intrinsically disordered proteins of the Nuclear Pore Complex. *eLife* **2016**, *5*, e10785.
- ³⁸ Lin, Y.-H.; Song, J.; Forman-Kay, J. D.; Chan, H. S. Random-phase-approximation theory for sequence-dependent, biologically functional liquid-liquid phase separation of intrinsically disordered proteins. *J. Mol. Liq.*, **2017**, *228*, 176–193.
- ³⁹ Lin, Y.-H.; Chan, H. S. Phase separation and single-chain compactness of charged disordered proteins are strongly correlated. *Biophys. J.* **2017**, *112*, 2043–2046.
- ⁴⁰ Dignon, G. L.; Zheng, W.; Kim, Y. C.; Best, R. B.; Mittal, J. Sequence determinants of protein phase behavior from a coarse-grained model. *PLoS Comput. Biol.* **2018**, *14*, e1005941.
- ⁴¹ Das, S.; Eisen, A.; Lin, Y.-H.; Chan, H. S. A lattice model of charge-pattern-dependent polyampholyte phase separation. *J. Phys. Chem. B* **2018**, *122*, 5418–5431.
- ⁴² Dignon, G. L.; Zheng, W.; Best, R. B.; Kim, Y. C.; Mittal, J. Relation between single-molecule properties and phase behavior of intrinsically disordered proteins. *Proc. Natl. Acad. Sci. U.S.A.* **2018**, *115*, 9929–9934.
- ⁴³ Das, S.; Amin, A. N.; Lin, Y.-H.; Chan, H. S. Coarse-grained residue-based models of disordered protein condensates: Utility and limitations of simple charge pattern parameters. *Phys. Chem. Chem. Phys.* **2018**, *20*, 28558–28574.
- ⁴⁴ Robichaud, N. A. S.; Saika-Voivod, I.; Wallin, S. Phase behavior of blocky charge lattice polymers: Crystals, liquids, sheets, filaments, and clusters. *Phys. Rev. E.* **2019**, *100*, 052404.
- ⁴⁵ Lin, Y.; McCarty, J.; Rauch, J. N.; Delaney, K. T.; Kosik, K. S.; Fredrickson, G. H.; Shea, J.-E.; Han, S. Narrow equilibrium window for complex coacervation of tau and RNA under cellular conditions *eLife* **2019**, *8*, e42571.
- ⁴⁶ McCarty, J.; Delaney, K. T.; Danielsen, S. P. O.; Fredrickson, G. H.; Shea, J.-E. Complete phase diagram for liquid-liquid phase separation of intrinsically disordered proteins. *J. Phys. Chem. Lett.* **2019**, *10*, 1644–1652.
- ⁴⁷ Leopold, P. E.; Montal, M.; Onuchic, J. N. Protein folding funnels: A kinetic approach to the

- sequence-structure relationship. *Proc. Natl. Acad. Sci. U.S.A.* **1992**, *89*, 8721–8725.
- ⁴⁸ Wolynes, P. G.; Onuchic, J. N.; Thirumalai, D. Navigating the folding routes. *Science* **1995**, *267*, 1619–1620.
- ⁴⁹ Dill, K. A.; Chan, H. S. From Levinthal to pathways to funnels. *Nat. Struct. Biol.* **1997**, *4*, 10–19.
- ⁵⁰ Klosin, A.; Oltsch, F.; Harmon, T.; Honigmann, A.; Jülicher, F.; Hyman, A. A.; Zechner, C. Phase separation provides a mechanism to reduce noise in cells. *Science* **2020**, *367*, 464–468.
- ⁵¹ Deviri, D.; Safran, S. A. Physical theory of biological noise buffering by multicomponent phase separation. *Proc. Natl. Acad. Sci. U.S.A.* **2021**, *118*, e2100099118.
- ⁵² Cinar, H.; Oliva, R.; Lin, Y.-H.; Chen, X.; Zhang, M.; Chan, H. S.; Winter, R. Pressure sensitivity of SynGAP/PSD-95 condensates as a model for postsynaptic densities and its biophysical and neurological ramifications. *Chem. Eur. J.* **2020**, *26*, 11024–11031.
- ⁵³ Cinar, H.; Oliva, R.; Wu, H.; Zhang, M.; Chan, H. S.; Winter, R. Effects of cosolvents and crowding agents on the stability and phase transition kinetics of the SynGAP/PSD-95 condensate model of postsynaptic densities. *J. Phys. Chem. B* **2022**, *126*, 1734–1741.
- ⁵⁴ Tsang, B.; Pritišanac, I.; Scherer, S. W.; Moses, A. M.; Forman-Kay, J. D. Phase separation as a missing mechanism for interpretation of disease mutations. *Cell* **2020**, *183*, 1742–1756.
- ⁵⁵ Flory, P. J. (1953) *Principles of Polymer Chemistry*; Cornell University Press:Ithaca, New York, 1953.
- ⁵⁶ Overbeek, J. T. G.; Voorn, M. J. Phase separation in polyelectrolyte solutions. Theory of complex coacervation. *J. Cell. Comp. Physiol.* **1957**, *49*, 7–26.
- ⁵⁷ Ermoshkin, A. V.; Olvera de la Cruz, M. A modified random phase approximation of polyelectrolyte solutions. *Macromolecules* **2003**, *36*, 7824–7832.
- ⁵⁸ Fredrickson, G. H. *The Equilibrium Theory Of Inhomogeneous Polymers*; Oxford University Press Inc.:New York, 2006.
- ⁵⁹ Danielsen, S. P. O.; McCarty, J.; Shea, J.-E.; Delaney, K. T.; Fredrickson, G. H. Molecular design of self-coacervation phenomena in block polyampholytes. *Proc. Natl. Acad. Sci. U.S.A.* **2019**, *116*, 8224–8232.
- ⁶⁰ Danielsen, S. P. O.; McCarty, J.; Shea, J.-E.; Delaney, K. T.; Fredrickson, G. H. Small ion effects on self-coacervation phenomena in block polyampholytes. *J. Chem. Phys.* **2019**, *151*, 034904.
- ⁶¹ Nilsson, D.; Irbäck, A. Finite-size scaling analysis of protein droplet formation. *Phys. Rev. E*, **2020**, *101*, 022413.
- ⁶² Pal, T.; Wessén, J.; Das, S.; Chan, H. S. Subcompartmentalization of polyampholyte species in organelle-like condensates is promoted by charge-pattern mismatch and strong excluded-volume interaction. *Phys. Rev. E* **2021**, *103*, 042406.
- ⁶³ Nilsson, D.; Irbäck, A. Finite-size shifts in simulated protein droplet phase diagrams. *J. Chem.*

- Phys.* **2021**, *154*, 235101.
- ⁶⁴ Nilsson, D.; Bozorg, B.; Mohanty, S.; Söderberg, B.; Irbäck, A. Limitations of field-theory simulation for exploring phase separation: The role of repulsion in a lattice protein model. *J. Chem. Phys.* **2022**, *156*, 015101.
- ⁶⁵ Choi, J.-M.; Dar, F.; Pappu, R. V. LASSI: A lattice model for simulating phase transitions of multivalent proteins. *PLoS Comput. Biol.* **2019**, *15*, e1007028.
- ⁶⁶ Das, S.; Lin, Y.-H.; Vernon, R. M.; Forman-Kay, J. D.; Chan, H. S. Comparative roles of charge, π , and hydrophobic interactions in sequence-dependent phase separation of intrinsically disordered proteins. *Proc. Natl. Acad. Sci. U.S.A.* **2020**, *117*, 28795–28805.
- ⁶⁷ Silmore, K. S.; Howard, M. P.; Panagiotopoulos, A. Z. Vapor-liquid equilibrium and surface tension of fully flexible Lennard-Jones chains. *Mol. Phys.* **2017**, *115*, 320–327.
- ⁶⁸ Regy, R. M.; Zheng, W.; Mittal, J. Using a sequence-specific coarse-grained model for studying protein liquid-liquid phase separation. *Methods Enzymol.* **2021**, *646*, 1–17.
- ⁶⁹ Rauscher, S.; Pomès, R. The liquid structure of elastin. *eLife* **2017**, *6*, e26526.
- ⁷⁰ Zheng, W.; Dignon, G. L.; Jovic, N.; Xu, X.; Regy, R. M.; Fawzi, N. L.; Kim, Y. C.; Best, R. B.; Mittal, J. Molecular details of protein condensates probed by microsecond long atomistic simulations. *J. Phys. Chem. B* **2020**, *124*, 11671–11679.
- ⁷¹ Lytle, T. K.; Sing, C. E. Transfer matrix theory of polymer complex coacervation. *Soft Matter*, **2017**, *13*, 7001–7012.
- ⁷² Chang, L.-W.; Lytle, T. K.; Radhakrishna, M.; Madinya, J. J.; Vélez, J.; Sing, C. E.; Perry, S. L. Sequence and entropy-based control of complex coacervates. *Nat. Comm.* **2017**, *8*, 1273.
- ⁷³ Sing, C. E.; Perry, S. L. Recent progress in the science of complex coacervation. *Soft Matter* **2020**, *16*, 2885–2914.
- ⁷⁴ Kastelic, M.; Kalyuzhnyi, Y. V.; Vlachy, V. Modeling phase transitions in mixtures of β - γ lens crystallins. *Soft Matter* **2016**, *12*, 7289–7298.
- ⁷⁵ Nguemaha, V.; Zhou, H.-X. Liquid-liquid phase separation of patchy particles illuminates diverse effects of regulatory components on protein droplet formation. *Sci. Rep.* **2018**, *8*, 6728.
- ⁷⁶ Espinosa, J. R.; Joseph, J. A.; Sanchez-Burgosa, I.; Garaizara, A.; Frenkel, D.; Collepardo-Guevara, R. Liquid network connectivity regulates the stability and composition of biomolecular condensates with many components. *Proc. Natl. Acad. Sci. U.S.A.*, **2020** *117*, 13238–13247.
- ⁷⁷ Wertheim, M. S. Fluids with highly directional attractive forces. IV. Equilibrium polymerization. *J. Stat. Phys.* **1986**, *42*, 477–492.
- ⁷⁸ Lin, Y.-H.; Wessén, J.; Pal, T.; Das, S.; Chan, H. S. Numerical techniques for applications of analytical theories to sequence-dependent phase separations of intrinsically disordered proteins. In *Phase-Separated Biomolecular Condensates, Methods and Protocols*; Zhou, H.-X.; Spille, J.-H.; Banerjee, P. R., Eds.; *Methods Mol. Biol.* (Springer-Nature), **2022**, *2563*, Chapter 3, pp. 51–94 [https://doi.org/10.1007/978-1-0716-2663-4_3] [Preprint (arXiv):

arXiv:2201.01920v3 [q-bio.BM]].

- ⁷⁹ Qian, D.; Michaels, T. C. T.; Knowles, T. P. J. Analytical solution to the Flory-Huggins model. *J. Phys. Chem. Lett.* **2022**, *13*, 7853–7860.
- ⁸⁰ Martin, E. W.; Holehouse, A. S.; Peran, I.; Farag, M.; Incicco, J. J.; Bremer, A.; Grace, C. R.; Soranno, A.; Pappu, R. V.; Mittag, T. Valence and patterning of aromatic residues determine the phase behavior of prion-like domains. *Science* **2020**, *367*, 694–699.
- ⁸¹ Amin, A. N.; Lin, Y.-H.; Das, S.; Chan, H. S. Analytical theory for sequence-specific binary fuzzy complexes of charged intrinsically disordered proteins. *J. Phys. Chem. B* **2020**, *124*, 6709–6720.
- ⁸² Hazra, M. K.; Levy, Y. Charge pattern affects the structure and dynamics of polyampholyte condensates. *Phys. Chem. Chem. Phys.* **2020**, *22*, 19368–19375.
- ⁸³ Alshareedah, I.; Moosa, M. M.; Raju, M.; Potoyan, D. A.; Banerjee, P. R. Phase transition of RNA-protein complexes into ordered hollow condensates. *Proc. Natl Acad. Sci. U. S. A.* **2020**, *117*, 15650–15658.
- ⁸⁴ Hazra, M. K.; Levy, Y. Affinity of disordered protein complexes is modulated by entropy-energy reinforcement. *Proc. Natl. Acad. Sci. U.S.A.* **2022**, *119*, e2120456119.
- ⁸⁵ Mohanty, P.; Kapoor, U.; Devarajan, D. S.; Phan, T. M.; Rizuan, A.; Mittal, J. Principles governing the phase separation of multidomain proteins. *Biochemistry* **2022** [doi: 10.1021/acs.biochem.2c00210].
- ⁸⁶ Sawle, L.; Ghosh, K. A theoretical method to compute sequence dependent configurational properties in charged polymers and proteins. *J. Chem. Phys.* **2015**, *143*, 085101.
- ⁸⁷ Lin, Y.-H.; Brady, J. P.; Chan, H. S.; Ghosh, K. A unified analytical theory of heteropolymers for sequence-specific phase behaviors of polyelectrolytes and polyampholytes. *J. Chem. Phys.* **2020**, *152*, 045102.
- ⁸⁸ Rumyantsev, A. M.; Johner, A.; Tirrell, M. V.; de Pablo, J. J. Unifying weak and strong charge correlations within the random phase approximation: Polyampholytes of various sequences. *Macromolecules* **2022**, *55*, 6260–6274.
- ⁸⁹ Das, R. K.; Pappu, R. V. Conformations of intrinsically disordered proteins are influenced by linear sequence distributions of oppositely charged residues. *Proc. Natl. Acad. Sci. U.S.A.* **2013**, *110*, 13392–13397.
- ⁹⁰ Ghosh, K.; Huihui, J.; Phillips, M.; Halder, A. Rules of physical mathematics govern intrinsically disordered proteins. *Annu. Rev. Biophys.* **2022**, *51*, 355–376.
- ⁹¹ Wessén, J.; Pal, T.; Das, S.; Lin, Y.-H.; Chan, H. S. A simple explicit-solvent model of polyampholyte phase behaviors and its ramifications for dielectric effects in biomolecular condensates. *J. Phys. Chem. B* **2021**, *125*, 4337–4358.
- ⁹² Wessén, J.; Pal, T.; Chan, H. S. Field theory description of ion association in phase separation of polyampholytes. *J. Chem. Phys.* **2022**, *156*, 194903.

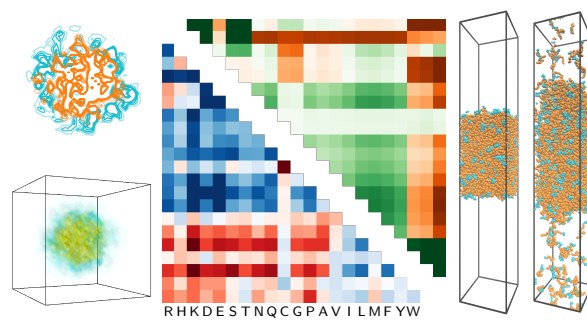
- ⁹³ Sawle, L.; Huihui, J.; Ghosh, K. All-atom simulations reveal protein charge decoration in the folded and unfolded ensemble is key in thermophilic adaptation. *J. Chem. Theory Comput.* **2017**, *13*, 5065–5075.
- ⁹⁴ Firman, T.; Ghosh, K. Sequence charge decoration dictates coil-globule transition in intrinsically disordered proteins. *J. Chem. Phys.* **2018**, *148*, 123305.
- ⁹⁵ Huihui, J.; Firman, T.; Ghosh, K. Modulating charge patterning and ionic strength as a strategy to induce conformational changes in intrinsically disordered proteins. *J. Chem. Phys.* **2018**, *149*, 085101.
- ⁹⁶ Huihui, J.; Ghosh, K. An analytical theory to describe sequence-specific inter-residue distance profiles for polyampholytes and intrinsically disordered proteins. *J. Chem. Phys.* **2020**, *152*, 161102.
- ⁹⁷ Song, J.; Ng, S. C.; Tompa, P.; Lee, K. A. W.; Chan, H. S. Polycation- π interactions are a driving force for molecular recognition by an intrinsically disordered oncoprotein family. *PLoS Comput. Biol.* **2013**, *9*, e1003239.
- ⁹⁸ Vernon, R. M.; Chong, P. A.; Tsang, B.; Kim, T. H.; Bah, A.; Farber, P.; Lin, H.; Forman-Kay, J. D. Pi-Pi contacts are an overlooked protein feature relevant to phase separation. *eLife* **2018**, *7*, e31486.
- ⁹⁹ Wang, J.; Choi, J. M.; Holehouse, A. S.; Lee, H. O.; Zhang, X.; Jahnel, M.; Maharana, S.; Lemaitre, R.; Pozniakovskiy, A.; Drechsel, D.; Poser, I.; Pappu, R. V.; Alberti, S.; Hyman, A. A. A molecular grammar governing the driving forces for phase separation of prion-like RNA binding proteins. *Cell* **2018**, *174*, 688–699.
- ¹⁰⁰ Li, S.; Yoshizawa, T.; Yamazaki, R.; Fujiwara, A.; Kameda, T.; Kitahara, R. Pressure and temperature phase diagram for liquid-liquid phase separation of the RNA-binding protein fused in sarcoma. *J. Phys. Chem. B* **2021**, *125*, 6821–6829.
- ¹⁰¹ Kamagata, K.; Ariefai, M.; Takahashi, H.; Hando, A.; Subekti, D. R. G.; Ikeda, K.; Hirano, A.; Kameda, T. Rational peptide design for regulating liquid-liquid phase separation on the basis of residue-residue contact energy. *Sci. Rep.* **2022**, *12*, 13718.
- ¹⁰² Zheng, W.; Dignon, G.; Brown, M.; Kim, Y. C.; Mittal, J. Hydrophathy patterning complements charge patterning to describe conformational preferences of disordered proteins. *J. Phys. Chem. Lett.* **2020**, *11*, 3408–3415.
- ¹⁰³ Song, J.; Li, J.; Chan, H. S. Small-angle X-ray scattering signatures of conformational heterogeneity and homogeneity of disordered protein ensembles. *J. Phys. Chem. B* **2021**, *125*, 6451–6478.
- ¹⁰⁴ Li, H.; Tang, C.; Wingreen, N. S. Nature of driving force for protein folding: A result from analyzing the statistical potential. *Phys. Rev. Lett.* **1997**, *79*, 765–768.
- ¹⁰⁵ Chan, H. S. Folding alphabets. *Nat. Struct. Biol.* **1999**, *6*, 994–996.
- ¹⁰⁶ Cieplak, M.; Holter, N. S.; Maritan, A.; Banavar, J. R. Amino acid classes and the protein

- folding problem. *J. Chem. Phys.* **2001**, *114*, 1420–1423.
- ¹⁰⁷ Norgaard, A. B.; Ferkinghoff-Borg, J.; Lindorff-Larsen, K. Experimental parameterization of an energy function for the simulation of unfolded proteins. *Biophys. J.* **2008**, *94*, 182–192.
- ¹⁰⁸ Kapcha, L. H.; Rossky, P. J. A simple atomic-level hydrophobicity scale reveals protein interfacial structure. *J. Mol. Biol.* **2014**, *426*, 484–498.
- ¹⁰⁹ Urry, D. W.; Gowda, D. C.; Parker, T. M.; Luan, C. H.; Reid, M. C.; Harris, C. M.; Pattanaik, A.; Harris, R. D. Hydrophobicity scale for proteins based on inverse temperature transitions. *Biopolymers* **1992**, *32*, 1243–1250.
- ¹¹⁰ Latham, A. P.; Zhang, B. Maximum entropy optimized force field for intrinsically disordered proteins. *J. Chem. Theory Comput.* **2020**, *16*, 773–781.
- ¹¹¹ Regy, R. M.; Thompson, J.; Kim, Y. C.; Mittal, J. Improved coarse-grained model for studying sequence dependent phase separation of disordered proteins. *Protein Sci.* **2021**, *30*, 1371–1379.
- ¹¹² Dannenhoffer-Lafage, T.; Best, R. B. A data-driven hydrophobicity scale for predicting liquid–liquid phase separation of proteins. *J. Phys. Chem. B* **2021**, *125*, 4046–4056.
- ¹¹³ Tesei, G.; Schulz, T. K.; Crehuet, R.; Lindorff-Larsen, K. Accurate model of liquid–liquid phase behavior of intrinsically disordered proteins from optimization of single-chain properties. *Proc. Natl. Acad. Sci. U. S. A.* **2021**, *118*, e2111696118.
- ¹¹⁴ Miyazawa, S.; Jernigan, R. L. Estimation of effective interresidue contact energies from protein crystal structures: quasi-chemical approximation. *Macromolecules* **1985**, *18*, 534–552.
- ¹¹⁵ Miyazawa, S.; Jernigan, R. L. Residue-residue potentials with a favourable contact pair term and an unfavourable high packing density term, for simulation and threading. *J. Mol. Biol.* **1996**, *256*, 623–644.
- ¹¹⁶ Kim, Y. C.; Hummer, G. Coarse-grained models for simulations of multiprotein complexes: Application to ubiquitin binding. *J. Mol. Biol.* **2008**, *375*, 1416–1433.
- ¹¹⁷ Joseph, J. A.; Reinhardt, A.; Aguirre, A.; Chew, P. Y.; Russell, K. O.; Espinosa, J. R.; Garaizar, A.; Collepardo-Guevara, R. Physics-driven coarse-grained model for biomolecular phase separation with near-quantitative accuracy. *Nat. Comput. Sci.* **2021**, *1*, 732–743.
- ¹¹⁸ Villegas, J. A.; Levy, E. D. A unified statistical potential reveals that amino acid stickiness governs nonspecific recruitment of client proteins into condensates. *Protein Sci.* **2022**, *31*, e4361.
- ¹¹⁹ Godzik, A.; Koliński, A.; Skolnick, J. Are proteins ideal mixtures of amino acids? Analysis of energy parameter sets. *Protein Sci.* **1995**, *4*, 2107–2117.
- ¹²⁰ Chan, H. S.; Kaya, H.; Shimizu, S. Computational methods for protein folding: Scaling a hierarchy of complexities. In *Current Topics in Computational Molecular Biology*; Jiang, T., Xu Y., Zhang, M. Q., Eds.; The MIT Press, Cambridge, Massachusetts, U.S.A., 2002, Chapter 16, pp 403–447.
- ¹²¹ Karplus, P. A. Hydrophobicity regained. *Protein Sci.* **1997**, *6*, 1302–1307.

- ¹²² DeVido, D. R.; Dorsey, J. G.; Chan, H. S.; Dill, K. A. Oil/water partitioning has a different thermodynamic signature when the oil solvent chains are aligned than when they are amorphous. *J. Phys. Chem. B* **1998**, *102*, 7272–7279.
- ¹²³ Fossat, M. J.; Zeng, X.; Pappu, R. V. Uncovering differences in hydration free energies and structures for model compound mimics of charged side chains of amino acids. *J. Phys. Chem. B* **2021**, *125*, 4148–4161.
- ¹²⁴ Lum, K.; Chandler, D.; Weeks, J. D. Hydrophobicity at small and large length scales. *J. Phys. Chem. B* **1999**, *103*, 4570–4577.
- ¹²⁵ Makowski, M.; Sobolewski, E.; Czaplewski, C.; Liwo, A.; Ołdziej, S.; No, J. H.; Scheraga, H. A. Simple physics-based analytical formulas for the potentials of mean force for the interaction of amino acid side chains in water. 3. Calculation and parameterization of the potentials of mean force of pairs of identical hydrophobic side chains. *J. Phys. Chem. B* **2007**, *111*, 2925–2931.
- ¹²⁶ Makowski, M.; Sobolewski, E.; Czaplewski, C.; Oldziej, S.; Liwo, A.; Scheraga, H. A. Simple physics-based analytical formulas for the potentials of mean force for the interaction of amino acid side chains in water. IV. Pairs of different hydrophobic side chains. *J. Phys. Chem. B* **2008**, *112*, 11385–11395.
- ¹²⁷ Chan, H. S.; Zhang, Z.; Wallin, S.; Liu, Z. Cooperativity, local-nonlocal coupling, and nonnative interactions: Principles of protein folding from coarse-grained models. *Annu. Rev. Phys. Chem.* **2011**, *62*, 301–326.
- ¹²⁸ Shimizu, S.; Chan, H. S. Configuration-dependent heat capacity of pairwise hydrophobic interactions. *J. Am. Chem. Soc.* **2001**, *123*, 2083–2084.
- ¹²⁹ Shimizu, S.; Chan, H. S. Origins of protein denatured state compactness and hydrophobic clustering in aqueous urea: Inferences from nonpolar potentials of mean force. *Proteins: Struct. Funct. Genet.* **2002**, *49*, 560–566.
- ¹³⁰ Chan, H. S.; Shimizu, S.; Kaya, H. Cooperativity principles in protein folding. *Methods Enzymol.* **2004**, *380*, 350–379.
- ¹³¹ Chan, H. S. Protein folding: Matching speed and locality. *Nature* **1998**, *392*, 761–763.
- ¹³² Statt, A.; Casademunt, H.; Brangwynne, C. P.; Panagiotopoulos, A. Z. Model for disordered proteins with strongly sequence-dependent liquid phase behavior. *J. Chem. Phys.* **2020**, *152*, 075101.
- ¹³³ Rana, U.; Brangwynne, C. P.; Panagiotopoulos, A. Z. Phase separation versus aggregation behavior for model disordered proteins. *J. Chem. Phys.* **2021**, *155*, 125101.
- ¹³⁴ Jorgenson, W. L.; Tirado-Rives, J. The OPLS [optimized potentials for liquid simulations] potential functions for proteins, energy minimizations for crystals of cyclic peptides and crambin. *J. Am. Chem. Soc.* **1988**, *110*, 1657–1666.
- ¹³⁵ Wang, Z.-G. Fluctuation in electrolyte solutions: The self energy. *Phys. Rev. E* **2010**, *81*, 021501.

- ¹³⁶ Riggleman, R. A.; Kumar, R.; Fredrickson, G. H. Investigation of the interfacial tension of complex coacervates using field-theoretic simulations. *J. Chem. Phys.* **2012**, *136*, 024903.
- ¹³⁷ Dill, K. A.; Alonso, D. O. V.; Hutchinson, K. Thermal stabilities of globular proteins. *Biochemistry* **1989**, *28*, 5439–5449.
- ¹³⁸ Kaya, H.; Chan, H. S. Simple two-state protein folding kinetics requires near-Levinthal thermodynamic cooperativity. *Proteins: Struct. Funct. Genet.* **2003**, *52*, 510–523.
- ¹³⁹ Dignon, G. L.; Zheng, W.; Kim, Y. C.; Mittal, J. Temperature-controlled liquid-liquid phase separation of disordered proteins. *ACS Cent. Sci.* **2019**, *5*, 821–830.
- ¹⁴⁰ Bragg, W. L.; Williams, E. J. The effect of thermal agitation on atomic arrangement in alloys. *Proc. Roy. Soc. A (London)* **1934**, *145*, 699–730.
- ¹⁴¹ Dill, K. A. Theory for the folding and stability of globular proteins. *Biochemistry* **1985**, *24*, 1501–1509.
- ¹⁴² Fredrickson, G. H.; Ganesan, V.; Drolet, F. Field-theoretic computer simulation methods for polymers and complex fluids. *Macromolecules* **2002**, *35*, 16–39.
- ¹⁴³ Parisi, G. On complex probabilities. *Phys. Lett. B* **1983**, *131*, 393–395.
- ¹⁴⁴ Klauder, J. R. A Langevin approach to fermion and quantum spin correlation functions. *J. Phys. A: Math. Gen.* **1983**, *16*, L317–L319.
- ¹⁴⁵ Parisi, G.; Wu, Y.-S. Perturbation theory without gauge fixing. *Scientia Sinica* **1981** *24*, 483–496.
- ¹⁴⁶ Chan, H. S.; Halpern, M. B. New ghost-free infrared-soft gauges. *Phys. Rev. D* **1986**, *33*, 540–547.
- ¹⁴⁷ Chan, H. S.; Halpern, M. B. Continuum-regularized quantum gravity. *Zeitschrift Für Physik C* **1987**, *36*, 669–693.
- ¹⁴⁸ Rumpf, H. Stochastic quantum gravity in D dimensions. *Prog. Theor. Phys.* **1993**, *111*, 63–81.
- ¹⁴⁹ Weeks, J. D.; Chandler, D.; Andersen, H. C. Role of repulsive forces in determining the equilibrium structure of simple liquids. *J. Chem. Phys.* **1971**, *54*, 5237–5247.
- ¹⁵⁰ Wang, X.; Ramírez-Hinestrosa, S.; Dobnikar, J.; Frenkel, D. The Lennard-Jones potential: when (not) to use it. *Phys. Chem. Chem. Phys.* **2020**, *22*, 10624–10633.
- ¹⁵¹ Weyman, A.; Mavrantzas, V. G.; Öttinger, H. C. Field-theoretic simulation beyond δ -interactions: Overcoming the inverse potential problem in auxiliary field models. *J. Chem. Phys.* **2021**, *155*, 024106.
- ¹⁵² Yukawa, H. On the interaction of elementary particles. I. *Proc. Phys.-Math. Soc. (Japan)* **1935**, *17*, 48–57.
- ¹⁵³ Riback, J. A.; Eeftens, J. M.; Lee, D. S. W.; Quinodoz, S. A.; Beckers, L.; Becker, L. A.; Brangwynne, C. P. Viscoelastic RNA entanglement and advective flow underlie nucleolar form and function. bioRxiv 2021.12.31.474660 **2022**, doi: <https://doi.org/10.1101/2021.12.31.474660>.
- ¹⁵⁴ Itzykson, C.; Zuber, J.-B. *Quantum Field Theory*; McGraw-Hill Inc.:New York, NY 1980.

- ¹⁵⁵ Tros, M.; Zheng, L.; Hunger, J.; Bonn, M.; Bonn, D.; Smits, G. J.; Woutersen, S. Picosecond orientational dynamics of water in living cells. *Nat. Commun.* **2017**, *8*, 1–7.
- ¹⁵⁶ Ashbaugh, H. S.; Hatch, H. W. Natively unfolded protein stability as a coil-to-globule transition in charge/hydrophobicity space. *J. Am. Chem. Soc.* **2008**, *130*, 9536–9542.
- ¹⁵⁷ Lau, K. F.; Dill, K. A. A lattice statistical mechanics model of the conformational and sequence spaces of proteins. *Macromolecules* **1989**, *22*, 3986–3997.
- ¹⁵⁸ O’Toole, E. M.; Panagiotopoulos, A. Z. Monte Carlo simulation of folding transitions of simple model proteins using a chain growth algorithm. *J. Chem. Phys.* **1992**, *97*, 8644–8652.
- ¹⁵⁹ Anderson, J. A.; Glaser, J.; Glotzer, S. C. HOOMD-blue: A Python package for high-performance molecular dynamics and hard particle Monte Carlo simulations. *Comput. Mater. Sci.* **2020**, *173*, 109363.
- ¹⁶⁰ Anderson, J. A.; Lorenz, C. D.; Travesset, A. General purpose molecular dynamics simulations fully implemented on graphics processing units. *J. Comput. Phys.* **2008**, *227*, 5342–5359.
- ¹⁶¹ Martyna, G. J.; Tobias, D. J.; Klein, M. L. Constant pressure molecular dynamics algorithms. *J. Chem. Phys.* **1994**, *101*, 4177–4189.
- ¹⁶² Tuckerman, M. E.; Alejandre, J.; López-Rendón, R.; Jochim, A. L.; Martyna, G. J. A Liouville-operator derived measure-preserving integrator for molecular dynamics simulations in the isothermal-isobaric ensemble. *J. Phys. A* **2006**, *39*, 5629–5651.
- ¹⁶³ LeBard, D. N.; Levine, B. G.; Mertmann, P.; Barr, S. A.; Jusufi, A.; Sanders, S.; Klein, M. L.; Panagiotopoulos, A. Z. Self-assembly of coarse-grained ionic surfactants accelerated by graphics processing units. *Soft Matter* **2012**, *8*, 2385–2397.
- ¹⁶⁴ Matsen, M. W.; Beardsley, T. M. Field-theoretic simulations for block copolymer melts using the partial saddle-point approximation. *Polymers* **2021**, *13*, 2437.
- ¹⁶⁵ Lennon, E. M.; Mohler, G. O.; Ceniceros, H. D.; Garcia-Cervera, C. J.; Fredrickson, G. H. Numerical solutions of the complex Langevin equations in polymer field theory. *Multiscale Modeling & Simulation* **2008**, *6*, 1347–1370.
- ¹⁶⁶ Cheung, M. S.; García, A. E.; Onuchic, J. N. Protein folding mediated by solvation: Water expulsion and formation of the hydrophobic core occur after the structural collapse. *Proc. Natl. Acad. Sci. U.S.A.* **2002**, *99*, 685–690.
- ¹⁶⁷ Liu, Z.; Chan, H. S. Desolvation is a likely origin of robust enthalpic barriers to protein folding. *J. Mol. Biol.* **2005**, *349*, 872–889.
- ¹⁶⁸ Kaya, H.; Uzunoğlu, Z.; Chan, H. S. Spatial ranges of driving forces are a key determinant of protein folding cooperativity and rate diversity. *Phys. Rev. E* **2013**, *88*, 044701.



TOC graphics